

1 **The cellular immune response to COVID-19 deciphered by single cell multi-omics across**
2 **three UK centres**

3
4 Emily Stephenson*¹, Gary Reynolds*¹, Rachel A Botting*¹, Fernando J Calero-Nieto*², Michael
5 Morgan*^{3,4}, Zewen Kelvin Tuong*^{5,6}, Karsten Bach*^{3,4}, Waradon Sungnak*⁶, Kaylee B Worlock⁷,
6 Masahiro Yoshida⁷, Natsuhiko Kumasaka⁶, Katarzyna Kania⁴, Justin Engelbert¹, Bayanne Olabi¹,
7 Jarmila Stremenova Spegarova⁸, Nicola K Wilson², Nicole Mende², Laura Jardine¹, Louis CS
8 Gardner¹, Issac Goh¹, Dave Horsfall¹, Jim McGrath¹, Simone Webb¹, Michael W. Mather¹, Rik
9 GH Lindeboom⁶, Emma Dann⁶, Ni Huang⁶, Krzysztof Polanski⁶, Elena Prigmore⁶, Florian Gothe⁸,
10 Jonathan Scott⁸, Rebecca P Payne⁸, Kenneth F Baker^{8,9}, Aidan T Hanrath^{8,10}, Ina CD Schim van
11 der Loeff⁸, Andrew S Barr¹⁰, Amada Sanchez-Gonzalez¹⁰, Laura Bergamaschi^{11,12}, Federica
12 Mescia^{11,12}, Josephine L Barnes⁷, Eliz Kilich¹³, Angus de Wilton¹³, Anita Saigal¹⁴, Aarash Saleh¹⁴,
13 Sam M Janes^{7,13}, Claire M Smith¹⁵, Nusayhah Gopee^{1,16}, Caroline Wilson^{1,17}, Paul Coupland⁴,
14 Jonathan M Coxhead¹, Vladimir Y Kiselev⁶, Stijn van Dongen⁶, Jaume Bacardit¹⁸, Hamish W
15 King^{6,19}, Cambridge Institute of Therapeutic Immunology and Infectious Disease-National
16 Institute of Health Research (CITIID-NIHR) COVID BioResource Collaboration, Anthony J
17 Rostron⁸, A John Simpson⁸, Sophie Hambleton⁸, Elisa Laurenti², Paul A Lyons^{11,12}, Kerstin B
18 Meyer^{6†}, Marko Z Nikolic^{7,13†}, Christopher JA Duncan^{8,10†}, Ken Smith^{11,12†}, Sarah A
19 Teichmann^{6,21†}, Menna R Clatworthy^{5,12,20,22†}, John C Marioni^{3,4,6†}, Berthold Gottgens^{2†}, Muzlifah
20 Haniffa^{1,6,9,16†}

21
22 Correspondence to: m.a.haniffa@ncl.ac.uk, bg200@cam.ac.uk, marioni@ebi.ac.uk,
23 mrc38@cam.ac.uk, st9@sanger.ac.uk

24
25 **Affiliations**

26 ¹Biosciences Institute, Newcastle University, Newcastle upon Tyne, UK

27 ²Wellcome - MRC Cambridge Stem Cell Institute, University of Cambridge, Cambridge, UK

28 ³European Molecular Biology Laboratory, European Bioinformatics Institute, Wellcome Genome
29 Campus, Cambridge, UK

30 ⁴Cancer Research UK Cambridge Institute, University of Cambridge, Cambridge, UK

31 ⁵Molecular Immunity Unit, Department of Medicine, University of Cambridge, Cambridge, UK

- 32 ⁶Wellcome Sanger Institute, Wellcome Genome Campus, Cambridge, UK
33 ⁷UCL Respiratory, Division of Medicine, University College London, London, UK
34 ⁸Translational and Clinical Research Institute, Newcastle University, Newcastle upon Tyne, UK
35 ⁹NIHR Newcastle Biomedical Research Centre, Newcastle Hospitals NHS Foundation Trust,
36 Newcastle upon Tyne, UK
37 ¹⁰Department of Infection and Tropical Medicine, Newcastle upon Tyne Hospitals NHS
38 Foundation, UK
39 ¹¹Cambridge Institute for Therapeutic Immunology and Infectious Disease, Jeffrey Cheah
40 Biomedical Centre, Cambridge Biomedical Campus, UK
41 ¹²Department of Medicine, University of Cambridge, Cambridge Biomedical Campus, UK
42 ¹³University College London Hospitals NHS Foundation Trust, London, UK
43 ¹⁴Royal Free Hospital NHS Foundation Trust, London, UK
44 ¹⁵UCL Great Ormond Street Institute of Child Health, London, UK
45 ¹⁶Department of Dermatology, Newcastle Hospitals NHS Foundation Trust, Newcastle upon Tyne,
46 UK
47 ¹⁷The Innovation Lab Integrated Covid Hub North East, Newcastle Upon Tyne, UK
48 ¹⁸School of Computing, Newcastle University, Newcastle Upon Tyne, UK
49 ¹⁹Centre for Immunobiology, Blizard Institute, Queen Mary University of London, London UK
50 ²⁰Cambridge Institute for Therapeutic Immunology and Infectious Disease, Cambridge
51 Biomedical Campus, Cambridge, UK
52 ²¹Theory of Condensed Matter Group, Cavendish Laboratory/Department of Physics, University
53 of Cambridge, Cambridge, UK
54 ²²NIHR Cambridge Biomedical Research Centre, Cambridge, UK

55

56 * equal contribution

57 † co-senior authors

58

59

60

61

62

63 **Abstract**

64

65 The COVID-19 pandemic, caused by SARS coronavirus 2 (SARS-CoV-2), has resulted in excess
66 morbidity and mortality as well as economic decline. To characterise the systemic host immune
67 response to SARS-CoV-2, we performed single-cell RNA-sequencing coupled with analysis of
68 cell surface proteins, providing molecular profiling of over 800,000 peripheral blood mononuclear
69 cells from a cohort of 130 patients with COVID-19. Our cohort, from three UK centres, spans the
70 spectrum of clinical presentations and disease severities ranging from asymptomatic to critical.
71 Three control groups were included: healthy volunteers, patients suffering from a non-COVID-19
72 severe respiratory illness and healthy individuals administered with intravenous
73 lipopolysaccharide to model an acute inflammatory response. Full single cell transcriptomes
74 coupled with quantification of 188 cell surface proteins, and T and B lymphocyte antigen receptor
75 repertoires have provided several insights into COVID-19: 1. a new non-classical monocyte state
76 that sequesters platelets and replenishes the alveolar macrophage pool; 2. platelet activation
77 accompanied by early priming towards megakaryopoiesis in immature haematopoietic
78 stem/progenitor cells and expansion of megakaryocyte-primed progenitors; 3. increased clonally
79 expanded CD8⁺ effector:effector memory T cells, and proliferating CD4⁺ and CD8⁺ T cells in
80 patients with more severe disease; and 4. relative increase of IgA plasmablasts in asymptomatic
81 stages that switches to expansion of IgG plasmablasts and plasma cells, accompanied with higher
82 incidence of BCR sharing, as disease severity increases. All data and analysis results are available
83 for interrogation and data mining through an intuitive web portal. Together, these data detail the
84 cellular processes present in peripheral blood during an acute immune response to COVID-19, and
85 serve as a template for multi-omic single cell data integration across multiple centers to rapidly
86 build powerful resources to help combat diseases such as COVID-19.

87

88 **Introduction**

89

90 The outbreak of coronavirus disease 2019 (COVID-19) was declared a global pandemic on 11
91 March 2020¹, and as of 12 January 2021 has led to over 91 million infections and 1.9 million
92 deaths worldwide². Common symptoms, which are often mild and transient, include cough, fever
93 and loss of taste and/or smell³. In a small proportion of those infected, symptoms can worsen and

94 lead to hospitalisation, with the elderly and those with comorbidities being most at risk⁴. In critical
95 cases, patients may develop acute respiratory distress syndrome (ARDS) necessitating intensive
96 care therapy, including endotracheal intubation and mechanical ventilation⁵. Clinical trials of
97 vaccines and therapeutics have been performed at an unprecedented pace⁶, leading to the
98 emergency authorisation of several vaccine candidates for susceptible populations in December
99 2020⁷. Treatment strategies under investigation include medication with anti-viral, anti-
100 inflammatory and immunomodulatory properties⁸.

101
102 The aetiologic agent of COVID-19 is a novel highly-infectious pathogenic coronavirus, severe
103 acute respiratory syndrome coronavirus 2 (SARS-CoV-2). This enveloped, positive-sense single-
104 stranded RNA betacoronavirus utilises the cell surface receptor angiotensin-converting enzyme 2
105 (ACE2) to enter host cells⁹. ACE2 is expressed in various barrier tissues, including nasal
106 epithelium, conjunctival epithelium and intestines, as well as internal organs, including alveoli of
107 the lung, heart, brain, kidney and the uterine-placental interface¹⁰. Neuropilin (NRP1), a cell
108 surface receptor expressed in respiratory and olfactory epithelium, can also facilitate SARS-CoV-
109 2 cellular entry¹¹. Patients with COVID-19 infection often have lymphopenia in association with
110 high neutrophil and platelet counts, parameters which may give prognostic indication¹².

111
112 Several studies have highlighted a complex network of peripheral blood immune responses in
113 COVID-19 infection, with the role of T cells during infection being an area of particular focus^{13,14}.
114 A reduction of absolute numbers of T cells linked with disease severity has been reported, as well
115 as a decrease in IFN- γ production by lymphocytes¹⁵. However, a significant expansion of highly
116 cytotoxic effector T cell subsets has also been found in patients with moderate disease¹⁶.
117 Additionally, higher expression of exhaustion markers PD-1 and Tim-3 on CD8⁺ T cells have been
118 described in patients receiving Intensive Care Unit (ICU) therapy¹⁷.

119
120 The response of myeloid cells and B cells have been less well explored in COVID-19. Emergency
121 myelopoiesis, driven by inflammation, is thought to arise as a way to prevent tissue damage^{18,19}.
122 In severe cases, dysregulation of myelopoiesis coupled with abnormal monocyte activation can
123 occur¹⁸, but the underlying mechanisms remain to be explored. Extrafollicular B cell activation is
124 present in critically ill patients but despite the high levels of SARS-CoV-2 specific antibodies and

125 antibody secreting cells, many of these patients do not recover from the disease¹⁴. Neutralising
126 antibodies are protective against infection and potentially confer immunity to reinfection, as
127 adoptive transfer of anti-SARS-CoV-2 monoclonal antibodies into naive animals were shown to
128 reduce virus replication and disease development²⁰. Vaccine-induced neutralising antibody titers
129 have been correlated with protection in nonhuman primates²¹, and recovered patients display
130 robust antibody responses correlated with neutralisation of authentic virus for at least several
131 months²².

132
133 In this study we combined single cell resolution analysis of transcriptomes, cell surface proteins
134 and lymphocyte antigen receptor repertoires to characterise the cellular immune response in
135 peripheral blood to COVID-19 across a range of disease severities, integrating results across three
136 UK medical centres.

137

138 **Results**

139

140 *Altered transcriptomic and surface protein profiles related to severity of COVID-19 infection*

141 To delineate the immune response to COVID-19 infection, we collected venous blood samples
142 from patients with asymptomatic, mild, moderate, severe and critical²³ COVID-19 infection across
143 three UK centres in Newcastle, Cambridge and London. Controls included healthy volunteers,
144 patients with a non-COVID-19 severe respiratory illness, and healthy volunteers administered with
145 intravenous lipopolysaccharide (IV-LPS) as a surrogate for an acute systemic bacterial
146 inflammatory response (**Fig. 1A, Supplementary Table 1**). We generated single cell
147 transcriptome data from peripheral blood mononuclear cells (PBMCs) of all individuals as well as
148 a census of cell surface proteins using a panel of 192 antibody derived tags (ADT) (**Fig. 1A,**
149 **Supplementary Table 2**). In total, following demultiplexing and doublet removal, we sequenced
150 1,141,860 cells from 143 samples with 850,100 cells passing quality control (min of 200 genes
151 and <10% mitochondrial reads/cell) (**Extended Data 1A**). The full scRNA-seq dataset was
152 integrated using Harmony²⁴ (**Fig. 1B**). There was good mixing of cells by the kBET statistic
153 calculated for each cluster across sample IDs (rejection rate improved from 0.62 to 0.36 following
154 integration, $p < 2.1 \times 10^{-8}$ by Wilcoxon paired signed rank test (**Extended Data 1B-C**)).

155

156 Following Leiden clustering, cells were manually annotated based on the RNA expression of
157 known marker genes. RNA-based annotation was supported by surface protein expression of
158 markers commonly employed in flow cytometry to discriminate PBMC subpopulations (**Extended**
159 **Data 1D**). We defined 18 cell subsets across the datasets (**Fig. 1B**), with an additional 27 cell states
160 identified following sub-clustering (**Fig. 1B, 2A, 3A-B, 4A-B**). Our annotation was further
161 validated using the Azimuth annotation tool for PBMC where more than 50% of the cells were
162 mapped and matched to a unique cluster in 32/33 of the clusters defined in the Azimuth PBMC
163 dataset (proliferating CD8 T cells mapped across two clusters). Clusters unique to our data include
164 proliferating monocytes, ILC subpopulations and isotype-specific plasma cells. (**Extended Data**
165 **1E**). Our complete COVID-19 peripheral blood multi-omic data is available through the web-
166 portal at <https://covid19cellatlas.org>.

167
168 We assessed how cell populations varied with severity of COVID-19 and observed a relative
169 expansion of proliferating lymphocytes, proliferating monocytes, platelets, and mobilized
170 haematopoietic stem/progenitor cells (HSPCs) with worsening disease. In the B cell compartment,
171 there was an expansion of plasmablasts in COVID-19 and an increase in B cells in severe and
172 critical disease. In contrast to these expansions, there were reductions in MAIT cells with disease
173 severity (**Fig. 1C, Extended Data 2A**). These changes were in keeping with the trends observed
174 in clinical blood lymphocyte, monocyte and platelet counts of COVID-19 patients (**Extended**
175 **Data 2B, Supplementary Table 3**). To assess the broader impacts of patient characteristics and
176 clinical metadata on the altered proportion of cell type/states, we used a Poisson linear mixed
177 model (see Methods and **Supplementary Note 1**) which predicted the COVID-19 swab result (BF
178 corrected LR $P=2.3 \times 10^{-4}$; see Methods), disease severity at blood sampling (BF corrected LR
179 $P=3.5 \times 10^{-7}$), and centre (contributed by increased RBC and reduced monocytes in the Cambridge
180 patient cohort; BF corrected LR $P=3.5 \times 10^{-142}$) as the main contributing factors to cell population
181 frequency among 7 different clinical/technical factors (**Extended Data 2C**). Further, we found
182 that PBMC composition varied depending on symptom duration, with increased relative frequency
183 of pDCs, NK cells, CD14+ and CD16+ monocytes (FDR 10%) and decreased relative frequency
184 of B cells, Tregs, RBCs, platelets and CD4 T cells with a longer symptomatic interval before
185 sampling (**Extended Data 2E**). Critically ill patients were sampled at later time points from onset
186 of symptoms than mild-moderate-severe patients, consistent with the protracted course of infection

187 in critical disease (**Extended Data 2D**). However, concordant changes according to symptom
188 duration were still found when excluding critical patients, indicating the additional influence of
189 symptom duration on peripheral immune cell changes in SARS-CoV-2 infection (**Extended Data**
190 **2F**).

191
192 We observed expression of Type I/III interferon response genes in monocytes, DCs and HSPCs
193 across the spectrum of COVID-19 severity, but not in patients challenged with IV-LPS, in keeping
194 with the importance of type I and III interferons in the innate immune response to viral infection
195 (**Fig. 1D**). Type I/III interferon response-related genes were recently identified as harbouring
196 association signals in a Genome Wide Association Study (GWAS) for COVID-19
197 susceptibility^{25,26}. Of the genes identified in this study, we found *IFNAR2* was both upregulated in
198 COVID-19 compared to healthy in most circulating cell types and highly expressed by
199 plasmablasts, monocytes and DCs (**Extended Data 2G**).

200
201 To provide information on the cytokine and chemokine context influencing peripheral immune
202 cells, we performed multiplexed analysis of 45 proteins in serum. Two contrasting cytokine
203 profiles were evident when comparing mild/moderate to severe/critical patients. CCL4, CXCL10,
204 IL7 and IL1A were associated with severe and critical disease, suggesting an augmented drive for
205 monocyte and NK lymphocyte recruitment as well as support for T cell activity/pathology
206 (**Extended Data 2H, Supplementary Table 4**).

207
208 To take advantage of the comprehensive protein expression data, we used Cydar²⁷ to characterise
209 how the immune landscape changes with disease severity based on surface protein expression. We
210 divided cells into phenotypic hyperspheres based on the expression of 188 proteins. We then
211 quantified the number of cells from each severity group within the hyperspheres, which allowed
212 us to identify 430 hyperspheres that differed significantly in abundance with increasing severity
213 (spatial FDR < 0.05, **Fig. 1E**). Examining the surface protein expression profiles post-hoc showed
214 that differentially abundant hyperspheres were present in all major immune compartments. In
215 particular, we found an increase in populations of B cells (CD19⁺/CD20⁺), plasma cells (CD38⁺)
216 and HSPCs (CD34⁺) as well as a previously reported remodelling of the myeloid compartment¹⁸
217 (**Fig. 1E**).

218 *Mononuclear phagocytes and haematopoietic stem progenitors*

219 Transcriptome and surface proteome analysis of blood mononuclear phagocytes identified known
220 DC subsets (pDC, ASDC, DC1, DC2, DC3) and several monocyte states (**Figs. 2A-B**). Three cell
221 states of CD14⁺ monocytes are present (proliferating, classical CD14⁺ and activated CD83⁺) in
222 addition to two CD14⁺CD16⁺ monocyte cell states (non-classical CD16⁺ and C1QA/B/C⁺) (**Figs.**
223 **2A-B**). Proliferating monocytes and DCs expressing *MKI67* and *TOP2A* are present in increasing
224 frequency with worsening severity of COVID-19 (**Figs. 2A-B**). In contrast, circulating numbers
225 of DC2 and DC3 are reduced. Proliferating monocytes have previously been identified by flow
226 cytometry of COVID-19 patients' blood¹⁹. Here, we add that they share an extended protein and
227 RNA expression profile with CD14⁺ monocytes (**Figs. 2A-B**). Proliferating DCs most closely
228 resemble DC2. *C1QA/B/C*-expressing CD16⁺ monocytes are present at a low frequency relative to
229 whole PBMC in healthy blood, but are expanded in COVID-19 and are the only source of C1
230 complement components in PBMCs (**Fig. 2B, Extended Data 3A**).

231
232 We previously demonstrated the egress of blood DCs and monocytes from blood to alveolar space
233 with rapid acquisition of a lung molecular profile following human inhalational LPS challenge²⁸.
234 To better understand the relationship between circulating and lung alveolar mononuclear
235 phagocytes in COVID-19, we compared the transcriptome profile of blood DCs and monocytes
236 with their bronchoalveolar lavage (BAL) counterparts during COVID-19 using recently published
237 data (GSE145926)²⁹ (**Extended Data 3B**). As expected, partition-based graph abstraction (PAGA)
238 suggests transcriptional similarity between healthy circulating CD14⁺ monocytes and healthy BAL
239 macrophages, in agreement with recent data demonstrating that BAL macrophages can arise from
240 circulating CD14⁺ monocytes (**Fig. 2C**)³⁰. However, there is a surprisingly greater transcriptional
241 similarity between BAL macrophages and the expanded population of circulating
242 C1QA/B/C⁺CD16⁺ monocytes in COVID-19 (**Fig. 2C**). These observations raise the possibility of
243 a differential origin of alveolar macrophages during health and COVID-19. Both BAL
244 macrophages and C1QA/B/C⁺CD16⁺ monocytes express *FCGR3A* and *C1QA/B/C* and are
245 enriched for expression of type I interferon response genes (**Fig. 2A**). Myeloid hyperinflammatory
246 response has been reported to mediate lung and peripheral tissue damage via secretion of
247 inflammatory cytokines such as IL-6 and TNF α in COVID-19. We evaluated the expression of
248 these cytokines and found that they are primarily expressed by tissue rather than blood

249 mononuclear phagocytes (**Fig. 2C**). Genes differentially expressed in CD83⁺ CD14⁺ monocytes
250 and BAL macrophages across pseudotime identified expression of *IL15*, which is produced in
251 response to viral infections to promote NK proliferation, and leukocyte recruiting chemokines
252 including *CCL2*, *CCL4*, *CCL7*, and *CCL8* upregulated by BAL macrophages (**Fig. 2D**).

253
254 Tissue DCs respond to local inflammation and pathogen challenge by migrating to the draining
255 lymph node to activate naïve T cells. BAL contains a population of mature, migratory DCs that
256 express *CCR7* and *LAMP3* but downregulate DC-specific markers such as *CD1C* and *CLEC9A*
257 (**Extended Data 3B**). These migratory DCs express *IL10* in healthy BAL but express *TNF* and the
258 common IL-12 and IL-23 subunit *IL12B* in COVID-19, suggesting altered capacity for T cell
259 polarisation (**Fig. 2E**). In peripheral blood, C1QA/B/C⁺CD16⁺ monocytes expressed the highest
260 amount of Type 1 IFN response genes compared to all peripheral blood myeloid cells (**Fig. 2F**).
261 We detected minimal TNF- or IL6-mediated JAK-STAT signaling pathway activation in
262 circulating monocytes and DCs but this was upregulated by COVID-19 BAL mononuclear
263 phagocytes (**Fig. 2F**).

264
265 Coagulation abnormalities and monocyte-platelet aggregates have been previously reported in
266 COVID-19 patients^{31,32} and we observe an expansion of platelets associated with disease severity
267 (**Fig. 1C**). This led us to investigate the receptor-ligand interactions predicted to mediate
268 monocyte-platelet interactions using CellPhoneDB, which identified ICAM1 interactions on
269 platelets with CD11a-c/CD18 primarily on C1QA/B/C⁺CD16⁺ monocytes and CD16⁺ monocytes
270 (**Fig. 2G**). This is accompanied by increased expression of surface proteins indicative of platelet
271 activation (**Fig. 2H**).

272
273 Our large dataset (850,100 PBMCs) allowed us to interrogate rare populations, including the HSPC
274 compartment. To this end, we selected all cells in clusters with significant expression of the HSPC
275 marker CD34, which resulted in a total of 3,085 HSPCs, following removal of minor clusters co-
276 expressing mature lineage markers. Leiden clustering and UMAP visualisation resulted in a cloud-
277 like representation with closely attached clusters, consistent with a stem/progenitor landscape
278 previously described for bone marrow HSPCs³³ (**Fig. 2I, Extended Data 3C**). Absence of CD38
279 mRNA and protein expression marks the most immature cells within the CD34 compartment,

280 while expression of markers such as *GATA1*, *MPO* and *PF4* characterises distinct erythroid,
281 myeloid and megakaryocytic progenitor populations (**Fig. 2I**). Accordingly, we were able to
282 annotate six transcriptional clusters as CD34⁺CD38⁻ HSPCs, CD34⁺CD38⁺ early progenitor
283 HSPCs, and CD34⁺ CD38⁺ erythroid, megakaryocytic and myeloid progenitors as well as a small
284 population distinguished by the expression of genes associated with cell cycle (S-phase) (**Fig. 2I**).
285

286 Following stratification by disease severity, the most noteworthy observation was that the
287 megakaryocyte progenitors were essentially absent in healthy and asymptomatic individuals, but
288 comprised approximately 5% of CD34⁺ cells in mild, moderate, severe and critical patients (**Fig.**
289 **2J**). Unlike the bone marrow, which contains rapidly cycling progenitors, the peripheral blood is
290 not thought to constitute a site for haematopoiesis³⁴, consistent with the low number of CD34⁺
291 cells expressing a cell cycle signature, which was furthermore restricted to genes associated with
292 S-phase (**Fig. 2I**). Disease-associated alterations of the circulating CD34⁺ progenitor cells are
293 therefore a likely reflection of COVID-19 mediated perturbation of the normal homeostatic
294 functioning of the bone marrow haematopoietic stem/progenitor compartment.

295
296 In light of our earlier observations of platelet activation and enhanced C1QA/B/C⁺CD16⁺
297 monocyte-platelet interactions (**Figs. 2G-H**), the appearance of CD34⁺ megakaryocyte progenitors
298 was of particular interest, as it suggested a rebalancing of the stem/progenitor compartment. The
299 overall number of these megakaryocyte progenitors however was low, prompting us to seek
300 additional evidence for reprogramming of immature haematopoiesis. To this end, we carried out
301 differential gene expression analysis between the megakaryocyte, myeloid and erythroid
302 progenitor clusters, and used the resulting gene lists to build gene signatures in order to interrogate
303 early activation or priming of lineage-specific transcriptional programs in the most immature
304 haematopoietic progenitor cell clusters (**Extended Data 3D**). This analysis showed activation of
305 the megakaryocyte progenitor signature in both the CD38⁻ and CD38⁺ HSPC populations (**Fig.**
306 **2K**), with less pronounced effects seen with the erythroid and myeloid signatures (**Extended Data**
307 **3E**). Of note, the megakaryocyte signature was also strongly induced in the asymptomatic patients,
308 which do not contain substantial numbers of CD34⁺ megakaryocyte progenitors in their peripheral
309 blood. Our earlier observation of increased platelet activation within the context of normal platelet
310 counts (**Fig. 2H, Extended Data 2B**) is therefore consistent with a model whereby exaggerated

311 megakaryopoiesis may be compensating for peripheral platelet consumption in COVID-19
312 patients. Of note, our HSPC compartment analysis suggests that immature haematopoiesis is also
313 affected in asymptomatic patients, but possibly through distinct differentiation and/or cell
314 mobilisation processes. Taken together, our data suggest that alterations in the cellular composition
315 and transcription programs of the stem/progenitor compartment contribute to the patho-
316 physiological response to SARS-CoV-2 infection.

317

318 *T-lymphocytes and TCR changes*

319 To further characterise T-lymphocytes during the infection, we re-clustered the T cell compartment
320 and identified 15 clusters of CD4 T cells, CD8 T cells, and innate-like T cells including $\gamma\delta$ T cells,
321 NKT cells, and MAIT cells across sample collection sites, donors and disease severity groups (**Fig.**
322 **3A, Extended Data 4**). Our cell annotation is based on both RNA and protein expression of marker
323 genes, as well as effector cytokines (**Figs. 3B-C**). In the CD4 T cell compartment, we identified
324 naïve CD4 T cells, central memory T cells (CD4 CM), effector memory T cells (CD4 EM),
325 activated CD4 T cells expressing IL-22 (CD4 IL22), Th1 cells, Th2 cells, Th17 cells, Treg cells,
326 and circulating T follicular helper cells (cTfh). In the CD8 compartment, we found naïve CD8 T
327 cells, effector/cytotoxic T cells (CD8 TE), and effector memory T cells (CD8 EM) (**Fig. 3A**).

328

329 Cellular composition of the T cell compartment varied between the healthy and infected groups
330 (**Fig. 3D**). Notably, based on their relative proportions and differential abundance testing (FDR
331 10%), we found activated CD4 expressing IL-22, circulating Tfh cells, Th1 cells, Treg cells, CD8
332 EM cells, and MAIT cells relatively enriched in patients with asymptomatic and mild infection
333 phenotype, with NKT, proliferating CD8 and CD4, and CD8 TE cells enriched in patients with
334 more severe phenotypes (**Fig. 3E, Extended Data 5A-B**). Moreover, we observed multiple cell
335 populations that displayed non-linear differences across severity phenotypes (proliferating CD4 &
336 CD8, CD8 TE, CD4 Th1, CD4 Th17, CD4 CM, IL-22⁺ CD4, Treg), illustrating the complex
337 compositional changes to peripheral T cells that occur with COVID-19 severity (**Fig. 3E,**
338 **Extended Data 5B**). Interestingly, the enrichment of Treg cells and IL-22 expressing CD4 T cells
339 in the patients with less severe disease (asymptomatic & mild) could be associated with immuno-
340 regulatory and tissue-protective responses that may restrict immunopathology (**Fig. 3E**) as IL-22
341 was previously shown to be involved in tissue protection in influenza A virus infection³⁵, and

342 associated with low viral load in the lung parenchyma of COVID-19 patients³⁶. The enrichment of
343 proliferating CD4⁺ and CD8⁺ T cells, which also express some exhaustion marker genes (*LAG3*,
344 *TOX*), could account for the previous observation of increased expression of exhaustion markers
345 on CD8⁺ T cells in patients with severe disease¹⁷.

346
347 To investigate T cell phenotype beyond differential abundance of T cell subsets, we performed
348 differential gene expression analysis across disease severity (FDR 1%) followed by gene set
349 enrichment analysis (GSEA) in each cell type and found enrichment of pathways associated with
350 inflammation and T cell activation across multiple T cell subsets, including *IL-2/STAT5* signaling,
351 *mTORC1* signaling, inflammatory response, interferon gamma response, and *IL-6/JAK/STAT3*
352 signaling (**Extended Data 5C**). Increases in activation and cytotoxic phenotype in the T cells from
353 COVID-19 patients stimulated *ex vivo* with SARS-CoV-2 peptide was confirmed independently
354 by protein expression of CD137 and CD107a using flow cytometry (**Extended Data 5D**).

355
356 Next, we interrogated TCR clonality and the relative proportions of specific T cell subsets within
357 clonally expanded T cells in different disease groups (**Fig. 3F**). As expected, among the COVID-
358 19 patients, effector CD8 T cells were the most clonally expanded, with enriched large clone sizes,
359 across different disease groups, and their relative proportion increased with disease severity (**Figs.**
360 **3F-G, Extended Data 5E-F**). Conversely, the relative proportion of clonally expanded effector
361 memory CD8 T cells decreased in patients with more severe disease (**Figs. 3F-G**). The ratio of
362 effector CD8 T cells to effector memory CD8 T cells correlated with disease severity (**Fig. 3G**),
363 suggesting that CD8 T cell differentiation outcome may contribute to both anti-viral protection
364 and immunopathology. This could be a result of the degree of inflammation set by innate immunity
365 in the first instance, resulting in biased CD8 differentiation into antigen-specific short-lived
366 effector CD8 T cells (equivalent to CD8 effector T cells in this study) *versus* memory precursor
367 effector CD8 T cells (equivalent to CD8 effector memory T cells in this study), as previously
368 reported in animal models³⁷.

369
370
371
372

373 *B-lymphocytes and BCR changes*

374 Re-clustering of B and plasma cells in isolation identified 9 clusters that were annotated according
375 to canonical marker expression (**Figs. 4A-B**), and appropriate enrichment of previously published
376 transcriptional signatures (**Extended Data 6A**). This included immature, naïve, switched and non-
377 switched memory B cells, and a cluster of cells that enriched for markers previously described in
378 exhausted memory B cells^{38,39} (**Figs. 4A-B, Extended Data 6A**). We also found a large population
379 of CD19/CD20-negative plasmablasts, with high expression of the proliferation marker *MKI67*, as
380 well as IgM⁺, IgG⁺, and IgA⁺ plasma cells (**Figs. 4A-B**). In patients with symptomatic COVID-
381 19, there was a significant expansion of plasmablasts and plasma cells compared with healthy
382 controls and LPS-treated subjects (**Fig. 4C, Extended Data 6B**). Notably, this phenomenon was
383 less evident in COVID-19 patients with asymptomatic disease. IgG plasma cells, in particular,
384 were expanded in symptomatic COVID-19 compared with other groups, and the magnitude of this
385 expansion increased with worsening disease severity from mild to severe disease but surprisingly,
386 was less evident in patients with critical disease (**Fig. 4C, Extended Data 6B**). When considering
387 plasmablasts and plasma cells using the V(D)J data, IgA⁺ cells were expanded in patients with
388 asymptomatic COVID-19 (**Fig. 4D**), suggestive of an effective mucosal humoral response in this
389 patient group. This is paralleled by the greatest expansion of circulating Tfh cells in asymptomatic
390 patients and underlined by the strong correlation between cTfh cells with plasma cells in
391 asymptomatic/mild patients (**Fig. 3E, 4E, Extended Data 5A-B**), suggesting a potential
392 contribution of coordinated T cells/B cells response to effective humoral anti-viral protection in
393 these patients that is lost in severe and critical disease. This is consistent with previous findings
394 relating to the requirement of Tfh cells for optimal antibody responses and high-quality
395 neutralising antibodies in viral infection⁴⁰.

396
397 To interrogate the effect of COVID-19 infection on humoral immune cells beyond differential
398 expansion of subsets, we performed GSEA in each cell type. *Interferon alpha response* and
399 *interferon gamma response* pathway genes were enriched in all B cell subsets in COVID-19
400 patients, but this response was generally more marked in patients with asymptomatic or mild
401 disease, and attenuated in severe and critical disease (**Fig. 4F, Extended Data 6C**). The magnitude
402 of type 1 interferon transcriptional response in B cells mirrored serum IFN- α levels, which were
403 highest in patients with mild disease (**Extended Data 2H**), suggesting that the low expression of

404 IFN response genes in B cells in severe or critical disease does not reflect an inability of B cells to
405 respond to IFN- α , but rather attenuation of IFN- α . This may be because the initial anti-viral
406 response has waned in patients with severe or critical disease or because these patients fail to
407 sustain adequate IFN- α production by myeloid cells and pDCs following symptom onset as
408 previously reported¹³. Longitudinal sampling would be required to distinguish these two
409 possibilities.

410
411 In asymptomatic patients, *TNFA signalling via NF-kB* pathway genes were also enriched in
412 immature, naïve and switched memory B cells, but decreased in immature B cells and plasma cells
413 in critical and severe disease (**Fig. 4F, Extended Data 6C**). Assessment of the leading-edge genes
414 in this pathway demonstrated their markedly higher expression in all B cell and plasmablast/cell
415 subsets in asymptomatic COVID-19 patients compared with those with symptomatic disease (**Fig.**
416 **4G, Extended Data 6D**). TNF α was barely detectable in COVID-19 serum samples and highest
417 in patients with moderate disease (**Extended Data 1E**), suggesting that another cytokine e.g. IL-6
418 or stimulus may be responsible for NF-kB activation in asymptomatic COVID-19 patients.

419
420 Hypoxia pathway genes were enriched in immature and naïve B cells only in asymptomatic
421 patients (**Fig. 4F, Extended Data 6C**). Since these individuals are unlikely to be hypoxic (given
422 their lack of symptoms) we postulated that this signature may reflect another hypoxia-inducible
423 factor (HIF) activating stimulus, which includes B cell receptor (BCR) cross-linking⁴¹. We
424 assessed the expression of genes associated with BCR activation, such as *CD79A/B*, and
425 downstream kinases such as *BTK* in B cell subsets. Overall, BCR activation-associated genes were
426 most highly expressed in B cells in healthy control cells, followed by asymptomatic COVID-19
427 patients, with lower expression observed in all symptomatic COVID-19 groups (**Fig. 4G,**
428 **Extended Data 6D**). BCR activation threshold is also modulated by immune tyrosine inhibitory
429 motif (ITIM)-containing receptors that recruit phosphatases, increasing the activation threshold of
430 B cells⁴². BCR inhibitory gene expression was limited, but *CD22* was detectable across B cell
431 subsets in asymptomatic COVID-19, whilst *FCGR2B*, *CD72* and *PTPN6* expression was evident
432 in severe COVID-19 B cells (**Fig. 4G, Extended Data 6D**). Together, this analysis suggests that
433 B cells in asymptomatic COVID-19 patients and those with mild disease have a more pronounced
434 response to interferons, increased NF-kB activation, and a higher expression of genes associated

435 with BCR activation signaling, suggesting a potential for greater BCR activation. This may
436 indicate that more avid responses early in disease prevent progression to a more severe phenotype,
437 or may merely reflect the immune response in the early phase of the disease. Longitudinal analysis
438 of patient samples would be required to address this question.

439
440 Following activation, B cells differentiate into antibody-producing plasma cells, accompanied by
441 a progressive increase in oxidative metabolism^{43,44}. We observed differences in metabolic gene
442 pathway expression in plasmablasts and plasma cells between disease severity categories, with
443 enrichment of *oxidative phosphorylation* pathway genes in critical and severe disease, but increase
444 in *glycolysis* pathway genes in asymptomatic patient plasmablasts (**Fig. 4F, Extended Data 6D**).

445
446 We next assessed BCR clonality using *dandelion*, a novel single cell BCR-sequencing analysis
447 package (see methods), and found significantly more clonal expansion in symptomatic COVID-
448 19 patients compared with those with asymptomatic disease or healthy controls (**Fig. 4H,**
449 **Extended Data 7A**). Expanded clonotypes were found across all major cell types with larger
450 clonotypes primarily present in plasmablast/plasma cell clusters (**Extended Data 8A-B**). Within
451 the expanded clonotypes, there was some evidence of class switching within symptomatic COVID
452 groups but not in the asymptomatic/healthy (**Extended Data 8C**). Some related BCRs were
453 present in different individuals, with more incidence of V-, J- gene usage and related amino acid
454 sequences of heavy and light chain CDR3s observed in patients with severe or critical disease, and
455 in patients within one of the clinical centres (Newcastle) (**Fig. 4I**), which could arise due to local
456 variants of the virus driving expansion of specific B cell clones. We note that none of these related
457 BCRs were found to be expanded in the individuals which was expected as only a relatively small
458 number of B cells per individual were sampled. It would have been extremely unlikely to find
459 exactly matching heavy- and light-chain sequences across different individuals (even when
460 allowing for somatic hypermutation variation) given the expected low coverage that arises from a
461 small number of cells (relative to bulk BCR sequencing). Finally, we observed disproportionate
462 distribution in clonotype size, whether considering expanded or all clonotypes, and increased BCR
463 mutation between male and female patients, with greater levels of both in females compared with
464 males (**Fig. 4J, Extended Data 7B**). These differences in clonal expansion of B cells are consistent
465 with previous reports of worse outcomes in COVID-19 in males^{45,46}.

466 We summarise the immunological cellular and molecular profiles observed in our study
467 highlighting known and new discoveries as well as the distinguishing features of asymptomatic
468 and milder disease from severe and critical disease (**Fig. 5**). Future longitudinal studies may enable
469 us to distinguish if the distinct responses in asymptomatic and milder disease prevent progression
470 to severe phenotypes.

471

472 **Discussion**

473 Our cross-sectional multi-omics peripheral blood mononuclear cell survey of ~130 COVID-19
474 patients and controls across three UK centres revealed several new insights into COVID-19
475 pathogenesis. Firstly, peripheral blood monocytes and DCs exhibit an interferon response to
476 infection and replenish peripheral tissue mononuclear phagocytes such as alveolar macrophages.
477 Secondly, the initial peripheral tissue inflammation and systemic response to COVID-19 is
478 accompanied by altered haematopoiesis that is mirrored in the peripheral circulation evidenced by
479 megakaryocyte-primed gene expression in the earliest CD34⁺CD38⁻ HSPCs, exaggerated
480 megakaryopoiesis and platelet activation. CD1QA/B/C⁺CD16⁺ monocytes co-express
481 receptor:ligands predicted to interact with platelets, supporting their intertwined role in tissue
482 thrombosis reported in COVID-19.

483

484 We reveal a balance in protective versus immunopathogenic adaptive immune responses in
485 COVID-19 patients. In patients with less severe disease, we found enrichment of circulating Tfh
486 cells, which were previously shown to also be involved in SARS-CoV-2 infection^{47,48} and Th1
487 cells, which could also confer anti-viral protection^{49,50}. Our findings suggest that an imbalance in
488 CD8 T cell differentiation, including the overexpansion of CD8 effector T cells which likely
489 include antigen-specific short-lived effector cells, could lead to uncontrolled inflammation and
490 immunopathology. Whether the reduced proportion of clonally expanded CD8 effector memory T
491 cells could lead to impaired memory responses in patients with more severe disease remains an
492 open question to be further investigated.

493

494 Similarly, in B cells, expansion of plasmablasts and plasma cells is less evident in critical than in
495 moderate and severe patients. This response is paralleled by the Tfh profile in COVID-19 patients
496 and is consistent with post-mortem observations showing a lack of GCs in lymph nodes and spleen

497 in patients with fatal COVID-19 and a decrease in Tfh⁴⁸. We observe a diminished IFN- α response
498 in critical and severe patients' B cell compartments, further emphasising a critical role of these
499 responses in outcomes, as previously reported in COVID-19 patients with anti-type I IFN
500 antibodies⁵¹. The presence of common BCRs in samples from one geographical region could
501 reflect local differences in viral strain, with increasing awareness of how viral mutations may
502 influence outcomes, as has been shown to be clinically important for viral transmission with the
503 B.1.1.7 strain^{52,53}.

504
505 Our cross-sectional study demonstrates valuable new insights from multi-omics profiling of
506 peripheral blood as a window to understand peripheral tissue inflammation, as well as bone
507 marrow and systemic responses to acute COVID-19 infection. Our large datasets and web portal
508 provide a foundational resource on COVID-19 for the research and clinical communities.

509

510

511 **Acknowledgements**

512 We acknowledge assistance from Peter Vegh, James Fletcher and David Dixon to the IV-LPS
513 study and funding from the Wellcome Human Cell Atlas Strategic Science Support
514 (WT211276/Z/18/Z). We acknowledge Bertrand Yeung and Kristopher "Kit" Nazor from
515 Biologend for helpful discussions in the optimisation of the CITE-Seq protocol. We acknowledge
516 Rachel Queen and Rafiqul Hussain from Newcastle University Genomics Core Facility for
517 technical assistance. We acknowledge Martin Prete for assistance with online data hosting and
518 interactivity. We thank NIHR BioResource volunteers for their participation, and gratefully
519 acknowledge NIHR BioResource centres, NHS Trusts and staff for their contribution. We thank
520 the National Institute for Health Research, NHS Blood and Transplant, and Health Data Research
521 UK as part of the Digital Innovation Hub Programme. The views expressed are those of the
522 author(s) and not necessarily those of the NHS, the NIHR or the Department of Health and Social
523 Care. M.H. is funded by Wellcome (WT107931/Z/15/Z), The Lister Institute for Preventive
524 Medicine and Newcastle NIHR Biomedical Research Centre (BRC); B.G. is funded by Wellcome
525 (206328/Z/17/Z), MRC (MR/S036113/1), and the Aging Biology Foundation. S.A.T. is funded by
526 Wellcome (WT206194), ERC Consolidator and EU MRG-Grammar awards. Z.K.T. and M.R.C.
527 are supported by a Medical Research Council Human Cell Atlas Research Grant (MR/S035842/1).

528 J.C.M. is supported by core funding from Cancer Research UK (C9545/A29580) and from the
529 European Molecular Biology Laboratory (EMBL). M.R.C. is supported by a Versus Arthritis Cure
530 Challenge Research Grant (21777), and an NIHR Research Professorship (RP-2017-08-ST2-002).
531 H.W.K. is supported by Sir Henry Wellcome PostDoctoral fellowship Wellcome Trust
532 (213555/Z/18/Z). K.B.M acknowledges funding from the Chan Zuckerberg Initiative (grant 2017-
533 174169) and from Wellcome (WT211276/Z/18/Z and Sanger core grant WT206194). M.Z.N.
534 acknowledges funding from a UKRI Innovation/Rutherford Fund Fellowship allocated by the
535 MRC and the UK Regenerative Medicine Platform (MR/5005579/1 to M.Z.N.). M.Z.N. and
536 K.B.M. have been funded by the Rosetrees Trust (M944). K.B.W. is funded by University College
537 London, Birkbeck MRC Doctoral Training Programme. J.L.B. acknowledges funding from the
538 MRC and the UK Regenerative Medicine Platform (MR/5005579/1). M.Y. is funded by The Jikei
539 University School of Medicine. K.F.B is funded by an NIHR Clinical Lectureship (CL-2017-01-
540 004). N.M. is supported by a DFG Research Fellowship (ME 5209/1-1). C.J.A.D is funded by
541 Wellcome (211153/Z/18/Z) and acknowledges support from the Barbour Foundation. This work
542 was partly funded by UKRI/NIHR through the UK Coronavirus Immunology Consortium (UK-
543 CIC).

544

545

546 **Author Contributions**

547 M.H., B.G., S.T., J.M., M.R.C., M.Z.N., K.M. conceived the study. A.J.S., A.J.R. conceived the
548 IV-LPS study. C.J.A.D., K.S., P.L., M.Z.N., E.K., A.dW., A.Sai., A.Sal., S.M.J., A.T.H., K.F.B.,
549 I.C.D.SvdL., L.C.S.G., A.S.B., A.S.G., L.B. recruited patients, collected samples and clinical
550 metadata. E.S., R.A.B., F.G., J.S., R.P.P., K.B.W., M.Y., J.L.B., N.M., F.J.C. isolated PBMCs.
551 R.A.B., E.S., K.B.W., M.Y., J.L.B., N.M., F.J.C-N. performed 10x and CITE-seq. E.S., J.E., K.K.
552 prepared sequencing libraries. E.P., J.C., P.C. conducted the sequencing. G.R., Z.K.T., K.B.,
553 M.M., W.S., N.K., S.vD., V.K., N.H., R.L., K.P., E.D. analysed the data. M.H., B.G., S.T., J.M.,
554 M.R.C., M.Z.N., K.M., G.R., Z.K.T., K.B., M.M., W.S., N.K., R.A.B., E.S., L.J., S.W., J.S.S.
555 interpreted the data. J.S.S. performed flow cytometry. E.S. performed multiplex cytokine analysis.
556 M.H., B.G., S.T., M.R.C., J.M., E.S., G.R., R.B., L.J., B.O., M.M., K.B., N.K., W.S., M.Z.N. wrote
557 the manuscript. N.M., L.C.S.G., S.W., K.F.B., F.M., C.W., J.M.C., H.W.K., S.H., E.L., K.B.M.,

558 K.S., edited the manuscript. Z.K.T., H.W.K. developed software (*dandelion*). J.McG., D.H.
559 developed the web portal.

560

561 **Data and materials availability**

562 The dataset from our study can be explored interactively through a web portal:
563 <https://covid19cellatlas.org>. The data object, as a h5ad file, can also be downloaded from the portal
564 page. The processed data is available to download from Array Express using accession number E-
565 MTAB-10026.

566

567 **Code availability**

568 All data analysis scripts are available on <https://github.com/scCOVID-19/COVIDPBMC>

569

570 **Competing interests statement**

571 SAT has received remunerations for consulting and Scientific Advisory Board work from
572 Genentech, Biogen, Roche and GlaxoSmithKline as well as Foresite Labs over the past three years.

573

574

575 **References**

576 1. Bedford, J. *et al.* COVID-19: towards controlling of a pandemic. *Lancet* **395**, 1015–1018

577 (2020).

578 2. John Hopkins University. COVID-19 map-Johns Hopkins Coronavirus Resource Center.

579 *Coronavirus Resource Center* <https://coronavirus.jhu.edu/map.html> (2020).

580 3. Chen, N. *et al.* Epidemiological and clinical characteristics of 99 cases of 2019 novel

581 coronavirus pneumonia in Wuhan, China: a descriptive study. *The Lancet* vol. 395 507–513

582 (2020).

- 583 4. Burki, T. K. Coronavirus in China. *The Lancet Respiratory Medicine* vol. 8 238 (2020).
- 584 5. Gibson, P. G., Qin, L. & Pua, S. H. COVID-19 acute respiratory distress syndrome
585 (ARDS): clinical features and differences from typical pre-COVID-19 ARDS. *Med. J. Aust.*
586 **213**, 54–56.e1 (2020).
- 587 6. Lurie, N., Saville, M., Hatchett, R. & Halton, J. Developing Covid-19 Vaccines at
588 Pandemic Speed. *N. Engl. J. Med.* **382**, 1969–1973 (2020).
- 589 7. Singh, J. A. & Upshur, R. E. G. The granting of emergency use designation to COVID-19
590 candidate vaccines: implications for COVID-19 vaccine trials. *Lancet Infect. Dis.* (2020)
591 doi:10.1016/S1473-3099(20)30923-3.
- 592 8. Babaei, F., Mirzababaei, M., Nassiri-Asl, M. & Hosseinzadeh, H. Review of registered
593 clinical trials for the treatment of COVID-19. *Drug Dev. Res.* **383**, 1813 (2020).
- 594 9. Hoffmann, M. *et al.* SARS-CoV-2 Cell Entry Depends on ACE2 and TMPRSS2 and Is
595 Blocked by a Clinically Proven Protease Inhibitor. *Cell* **181**, 271–280.e8 (2020).
- 596 10. Sungnak, W. *et al.* SARS-CoV-2 entry factors are highly expressed in nasal epithelial cells
597 together with innate immune genes. *Nat. Med.* **26**, 681–687 (2020).
- 598 11. Cantuti-Castelvetri, L. *et al.* Neuropilin-1 facilitates SARS-CoV-2 cell entry and infectivity.
599 *Science* (2020) doi:10.1126/science.abd2985.
- 600 12. Jimeno, S. *et al.* Prognostic implications of neutrophil-lymphocyte ratio in COVID-19. *Eur.*
601 *J. Clin. Invest.* **51**, e13404 (2021).
- 602 13. Arunachalam, P. S. *et al.* Systems biological assessment of immunity to mild versus severe
603 COVID-19 infection in humans. *Science* **369**, 1210–1220 (2020).
- 604 14. Woodruff, M. C. *et al.* Extrafollicular B cell responses correlate with neutralizing antibodies
605 and morbidity in COVID-19. *Nat. Immunol.* **21**, 1506–1516 (2020).

- 606 15. Chen, G. *et al.* Clinical and immunological features of severe and moderate coronavirus
607 disease 2019. *J. Clin. Invest.* **130**, 2620–2629 (2020).
- 608 16. Zhang, J.-Y. *et al.* Single-cell landscape of immunological responses in patients with
609 COVID-19. *Nat. Immunol.* **21**, 1107–1118 (2020).
- 610 17. Diao, B. *et al.* Reduction and Functional Exhaustion of T Cells in Patients With
611 Coronavirus Disease 2019 (COVID-19). *Front. Immunol.* **11**, 827 (2020).
- 612 18. Schulte-Schrepping, J. *et al.* Severe COVID-19 Is Marked by a Dysregulated Myeloid Cell
613 Compartment. *Cell* **182**, 1419–1440.e23 (2020).
- 614 19. Mann, E. R. *et al.* Longitudinal immune profiling reveals key myeloid signatures associated
615 with COVID-19. *Sci Immunol* **5**, (2020).
- 616 20. Shi, R. *et al.* A human neutralizing antibody targets the receptor-binding site of SARS-
617 CoV-2. *Nature* **584**, 120–124 (2020).
- 618 21. Yu, J. *et al.* DNA vaccine protection against SARS-CoV-2 in rhesus macaques. *Science*
619 **369**, 806–811 (2020).
- 620 22. Wajnberg, A. *et al.* Robust neutralizing antibodies to SARS-CoV-2 infection persist for
621 months. *Science* **370**, 1227–1230 (2020).
- 622 23. Clinical management of COVID-19. [https://www.who.int/publications/i/item/clinical-](https://www.who.int/publications/i/item/clinical-management-of-covid-19)
623 [management-of-covid-19](https://www.who.int/publications/i/item/clinical-management-of-covid-19).
- 624 24. Korsunsky, I. *et al.* Fast, sensitive and accurate integration of single-cell data with
625 Harmony. *Nat. Methods* **16**, 1289–1296 (2019).
- 626 25. Severe Covid-19 GWAS Group *et al.* Genomewide Association Study of Severe Covid-19
627 with Respiratory Failure. *N. Engl. J. Med.* **383**, 1522–1534 (2020).
- 628 26. Pairo-Castineira, E. *et al.* Genetic mechanisms of critical illness in Covid-19. *Nature* (2020)

- 629 doi:10.1038/s41586-020-03065-y.
- 630 27. Lun, A. T. L., Richard, A. C. & Marioni, J. C. Testing for differential abundance in mass
631 cytometry data. *Nat. Methods* **14**, 707–709 (2017).
- 632 28. Jardine, L. *et al.* Lipopolysaccharide inhalation recruits monocytes and dendritic cell
633 subsets to the alveolar airspace. *Nat. Commun.* **10**, 1999 (2019).
- 634 29. Liao, M. *et al.* Single-cell landscape of bronchoalveolar immune cells in patients with
635 COVID-19. *Nat. Med.* **26**, 842–844 (2020).
- 636 30. Evren, E. *et al.* Distinct developmental pathways from blood monocytes generate human
637 lung macrophage diversity. *Immunity* (2020) doi:10.1016/j.immuni.2020.12.003.
- 638 31. Levi, M., Thachil, J., Iba, T. & Levy, J. H. Coagulation abnormalities and thrombosis in
639 patients with COVID-19. *The Lancet Haematology* vol. 7 e438–e440 (2020).
- 640 32. Hottz, E. D. *et al.* Platelet activation and platelet-monocyte aggregate formation trigger
641 tissue factor expression in patients with severe COVID-19. *Blood* **136**, 1330–1341 (2020).
- 642 33. Velten, L. *et al.* Human haematopoietic stem cell lineage commitment is a continuous
643 process. *Nat. Cell Biol.* **19**, 271–281 (2017).
- 644 34. Mende, N. *et al.* Quantitative and molecular differences distinguish adult human medullary
645 and extramedullary haematopoietic stem and progenitor cell landscapes.
646 doi:10.1101/2020.01.26.919753.
- 647 35. Ivanov, S. *et al.* Interleukin-22 reduces lung inflammation during influenza A virus
648 infection and protects against secondary bacterial infection. *J. Virol.* **87**, 6911–6924 (2013).
- 649 36. Desai, N. *et al.* Temporal and spatial heterogeneity of host response to SARS-CoV-2
650 pulmonary infection. *Nat. Commun.* **11**, 6319 (2020).
- 651 37. Joshi, N. S. *et al.* Inflammation directs memory precursor and short-lived effector CD8(+) T

- 652 cell fates via the graded expression of T-bet transcription factor. *Immunity* **27**, 281–295
653 (2007).
- 654 38. Monaco, G. *et al.* RNA-Seq Signatures Normalized by mRNA Abundance Allow Absolute
655 Deconvolution of Human Immune Cell Types. *Cell Rep.* **26**, 1627–1640.e7 (2019).
- 656 39. Adlowitz, D. G. *et al.* Expansion of Activated Peripheral Blood Memory B Cells in
657 Rheumatoid Arthritis, Impact of B Cell Depletion Therapy, and Biomarkers of Response.
658 *PLoS One* **10**, e0128269 (2015).
- 659 40. Crotty, S. T Follicular Helper Cell Biology: A Decade of Discovery and Diseases. *Immunity*
660 **50**, 1132–1148 (2019).
- 661 41. Meng, X. *et al.* Hypoxia-inducible factor-1 α is a critical transcription factor for IL-10-
662 producing B cells in autoimmune disease. *Nat. Commun.* **9**, 251 (2018).
- 663 42. Pritchard, N. R. & Smith, K. G. C. B cell inhibitory receptors and autoimmunity.
664 *Immunology* **108**, 263–273 (2003).
- 665 43. Doughty, C. A. *et al.* Antigen receptor-mediated changes in glucose metabolism in B
666 lymphocytes: role of phosphatidylinositol 3-kinase signaling in the glycolytic control of
667 growth. *Blood* **107**, 4458–4465 (2006).
- 668 44. Boothby, M. & Rickert, R. C. Metabolic Regulation of the Immune Humoral Response.
669 *Immunity* **46**, 743–755 (2017).
- 670 45. Guan, W.-J. *et al.* Clinical Characteristics of Coronavirus Disease 2019 in China. *N. Engl. J.*
671 *Med.* **382**, 1708–1720 (2020).
- 672 46. Onder, G., Rezza, G. & Brusaferro, S. Case-Fatality Rate and Characteristics of Patients
673 Dying in Relation to COVID-19 in Italy. *JAMA* **323**, 1775–1776 (2020).
- 674 47. Rydyznski Moderbacher, C. *et al.* Antigen-Specific Adaptive Immunity to SARS-CoV-2 in

- 675 Acute COVID-19 and Associations with Age and Disease Severity. *Cell* **183**, 996–1012.e19
676 (2020).
- 677 48. Kaneko, N. *et al.* Loss of Bcl-6-Expressing T Follicular Helper Cells and Germinal Centers
678 in COVID-19. *Cell* **183**, 143–157.e13 (2020).
- 679 49. Maloy, K. J. *et al.* CD4(+) T cell subsets during virus infection. Protective capacity depends
680 on effector cytokine secretion and on migratory capability. *J. Exp. Med.* **191**, 2159–2170
681 (2000).
- 682 50. Sahin, U. *et al.* COVID-19 vaccine BNT162b1 elicits human antibody and TH1 T cell
683 responses. *Nature* **586**, 594–599 (2020).
- 684 51. Bastard, P. *et al.* Autoantibodies against type I IFNs in patients with life-threatening
685 COVID-19. *Science* **370**, (2020).
- 686 52. Korber, B. *et al.* Tracking Changes in SARS-CoV-2 Spike: Evidence that D614G Increases
687 Infectivity of the COVID-19 Virus. *Cell* **182**, 812–827.e19 (2020).
- 688 53. Young, B. E. *et al.* Effects of a major deletion in the SARS-CoV-2 genome on the severity
689 of infection and the inflammatory response: an observational cohort study. *Lancet* **396**,
690 603–611 (2020).
- 691 54. Hay, S. B., Ferchen, K., Chetal, K., Grimes, H. L. & Salomonis, N. The Human Cell Atlas
692 bone marrow single-cell interactive web portal. *Exp. Hematol.* **68**, 51–61 (2018).
- 693 55. Dobin, A. *et al.* STAR: ultrafast universal RNA-seq aligner. *Bioinformatics* **29**, 15–21
694 (2013).
- 695 56. Heaton, H. *et al.* Souporecell: robust clustering of single-cell RNA-seq data by genotype
696 without reference genotypes. *Nat. Methods* **17**, 615–620 (2020).
- 697 57. McGinnis, C. S., Murrow, L. M. & Gartner, Z. J. DoubletFinder: Doublet Detection in

- 698 Single-Cell RNA Sequencing Data Using Artificial Nearest Neighbors. *Cell Syst* **8**, 329–
699 337.e4 (2019).
- 700 58. Haghverdi, L., Lun, A. T. L., Morgan, M. D. & Marioni, J. C. Batch effects in single-cell
701 RNA-sequencing data are corrected by matching mutual nearest neighbors. *Nat. Biotechnol.*
702 **36**, 421–427 (2018).
- 703 59. Büttner, M., Miao, Z., Wolf, F. A., Teichmann, S. A. & Theis, F. J. A test metric for
704 assessing single-cell RNA-seq batch correction. *Nat. Methods* **16**, 43–49 (2019).
- 705 60. Vento-Tormo, R. *et al.* Single-cell reconstruction of the early maternal-fetal interface in
706 humans. *Nature* **563**, 347–353 (2018).
- 707 61. Liberzon, A. *et al.* The Molecular Signatures Database (MSigDB) hallmark gene set
708 collection. *Cell Syst* **1**, 417–425 (2015).
- 709 62. Korotkevich, G., Sukhov, V. & Sergushichev, A. Fast gene set enrichment analysis.
710 doi:10.1101/060012.
- 711 63. Blondel, V. D., Guillaume, J.-L., Lambiotte, R. & Lefebvre, E. Fast unfolding of
712 communities in large networks. *Journal of Statistical Mechanics: Theory and Experiment*
713 vol. 2008 P10008 (2008).
- 714 64. McInnes, L., Healy, J. & Melville, J. UMAP: Uniform Manifold Approximation and
715 Projection for Dimension Reduction. *arXiv [stat.ML]* (2018).
- 716 65. Robinson, M. D., McCarthy, D. J. & Smyth, G. K. edgeR: a Bioconductor package for
717 differential expression analysis of digital gene expression data. *Bioinformatics* **26**, 139–140
718 (2010).
- 719 66. McCarthy, D. J., Chen, Y. & Smyth, G. K. Differential expression analysis of multifactor
720 RNA-Seq experiments with respect to biological variation. *Nucleic Acids Res.* **40**, 4288–

- 721 4297 (2012).
- 722 67. Kuleshov, M. V. *et al.* Enrichr: a comprehensive gene set enrichment analysis web server
723 2016 update. *Nucleic Acids Res.* **44**, W90–7 (2016).
- 724 68. Benjamini, Y. & Hochberg, Y. Controlling the False Discovery Rate: A Practical and
725 Powerful Approach to Multiple Testing. *J. R. Stat. Soc. Series B Stat. Methodol.* **57**, 289–
726 300 (1995).
- 727 69. Ghazanfar, S., Strbenac, D., Ormerod, J. T., Yang, J. Y. H. & Patrick, E. DCARS:
728 differential correlation across ranked samples. *Bioinformatics* **35**, 823–829 (2019).
- 729 70. Gupta, N. T. *et al.* Change-O: a toolkit for analyzing large-scale B cell immunoglobulin
730 repertoire sequencing data. *Bioinformatics* **31**, 3356–3358 (2015).
- 731 71. Lefranc, M.-P. IMGT, the International ImmunoGeneTics Information System® ,
732 <http://imgt.cines.fr>. *Novartis Foundation Symposia* 126–142 (2008)
733 doi:10.1002/0470090766.ch9.
- 734 72. Gadala-Maria, D., Yaari, G., Uduman, M. & Kleinstein, S. H. Automated analysis of high-
735 throughput B-cell sequencing data reveals a high frequency of novel immunoglobulin V
736 gene segment alleles. *Proc. Natl. Acad. Sci. U. S. A.* **112**, E862–70 (2015).
- 737 73. Bashford-Rogers, R. J. M. *et al.* Network properties derived from deep sequencing of
738 human B-cell receptor repertoires delineate B-cell populations. *Genome Res.* **23**, 1874–1884
739 (2013).

740

741

742 **Figure Legends**

743

744 **Figure 1: Single cell multi-omic analysis of COVID-19 patients' PBMC**

745 **A.** Overview of the participants included and the samples and data collected. IV-LPS, intravenous
746 lipopolysaccharide; PBMC, peripheral blood mononuclear cells. **B.** UMAP visualisation of all
747 850,100 cells sequenced. Leiden clusters based on 5' gene expression shown and coloured by cell
748 type. DC, dendritic cell; HSPC, haematopoietic stem and progenitor cell; lymph, lymphocyte;
749 MAIT, mucosal-associated invariant T cell; mono, monocyte; pDC, plasmacytoid dendritic cell;
750 Prolif., proliferating; RBC, red blood cell; NK, natural killer cell. **C.** Bar plot of the proportion of
751 cell types shown in **B.** separated by condition and COVID-19 severity status. Hypothesis testing
752 was performed using quasi-likelihood F-test comparing healthy controls to cases for linear trends
753 across disease severity groups (healthy > asymptomatic > mild > moderate > severe > critical).
754 Differentially abundant cell types were determined using a 10% false discovery rate (FDR) and
755 marked (*). **D.** Enrichment of interferon response of each cell state separated by severity. IFN
756 response was calculated using a published gene list (GO: 0034340) **E.** UMAP computed using
757 batch-corrected mean staining intensities of 188 antibodies for 4241 hyperspheres. Each
758 hypersphere represents an area in the 188-dimensional space and is colored by significant (spatial
759 $FDR < 0.05$) severity associated changes in abundance of cells within that space.

760

761 **Figure 2: Myeloid and progenitor cells**

762 **A.** Dot plots of gene expression (left; blue) and surface protein (right; red) expression for myeloid
763 populations where the colour is scaled by mean expression and the dot size is proportional to the
764 percent of the population expressing the gene/protein, respectively. **B.** Bar plot of the proportion
765 of myeloid populations separated by condition and severity status from the Ncl and Sanger/UCL
766 site. Hypothesis testing was performed using quasi-likelihood F-test comparing healthy controls
767 to cases. Differentially abundant cell types were determined using a 10% false discovery rate
768 (FDR) and marked (*). **C.** Partition based graph abstraction (PAGA) representing connectivity
769 between clusters defined in **A** for healthy (top left) and COVID-19 (bottom left) monocytes and
770 BAL macrophages. Expression of *IL6* (top right) and *TNF* (bottom right) in each cluster along the
771 predicted path for COVID-19 monocytes. **D.** Expression of differentially expressed cytokines
772 between $CD83^+CD14^+$ monocytes and BAL macrophages shown by cells ordered by pseudotime

773 calculated for COVID-19 monocytes and BAL macrophages from **C. E.** Expression of DC-derived
774 T cell polarising cytokines in peripheral blood DC2 and mature BAL DCs. **F.** Heat map displaying
775 gene set enrichment scores for Type 1/3 IFN-response, TNF-response and JAK-STAT signatures
776 in the myeloid populations found in COVID-19 PBMCs. **G.** Heat map of CellPhoneDB predicted
777 ligand:receptor interactions between platelets and monocyte subsets. **H.** Violin plots showing
778 significantly differentially expressed markers of platelet activation proteins between healthy and
779 COVID-19. **I.** UMAP representation of HSPCs (top) and gene expression markers used to annotate
780 clusters (below). MK, Megakaryocyte **J.** Bar chart of the proportion of progenitors by severity
781 status. MK, Megakaryocyte. **K.** Bar charts displaying enrichment of a megakaryocyte signature
782 found in CD34⁻CD38⁻ (left) and CD34⁺CD38⁺ HSPCs (right), separated by severity. MK,
783 megakaryocyte.

784

785 **Figure 3: T lymphocytes**

786 **A.** UMAP visualisation of T cells. Semi-supervised annotation of Louvain clusters based on gene
787 expression shown and coloured by cell type. CM, central memory; EM, effector memory; TE,
788 terminal effector; Th, T helper; Tfh, T follicular helper. Inset panels show the 2-dimensional kernel
789 density estimates of select T cell types in UMAP space. **B.** Dot plots of gene expression (top; blue)
790 and surface protein (bottom; red) expression for populations shown in **A.** where the colour is scaled
791 by mean expression and the dot size is proportional to the percent of the population expressing the
792 gene/protein, respectively. **C.** Dot plots of gene expression of cytokine genes for populations
793 shown in **A.** where the colour is scaled by mean expression and the dot size is proportional to the
794 percent of the population expressing the gene/protein, respectively. **D.** Box plots of cell type
795 proportions that are differentially abundant between healthy donors and COVID-19 cases. Boxes
796 denote interquartile range (IQR) with the median shown as horizontal bars. Whiskers extend to
797 1.5x the IQR; outliers are shown as individual points. **E.** Box plots of the proportion of cell types
798 shown in **A.** separated by severity status. Only cell types showing trends of changes with respect
799 to severity status are shown here. Boxes denote interquartile range (IQR) with the median shown
800 as horizontal bars. Whiskers extend to 1.5x the IQR; outliers are shown as individual points. **F.**
801 Bar plots showing the frequency of clonal T cells by severity. Expanded clones denote TCR
802 clonotypes observed more than once. Stars in key indicate significance after multiple testing
803 correction (Logistic regression; * $P < 0.05$, ** $P < 0.01$, *** $P < 0.001$).

804 proportion of clonally expanded effector memory CD8 T cells (left), effector CD8 T cells (middle),
805 and the ratio of effector CD8 T cells to effector memory CD8 T cells (right). Boxes denote
806 interquartile range (IQR) with the median shown as horizontal bars. Whiskers extend to 1.5x the
807 IQR; outliers are shown as individual points.

808

809 **Figure 4: B lymphocytes**

810 **A.** UMAP visualisation of 74,019 cells in the B cell lineage and coloured by cell type identified
811 from clustering on the gene expression data. **B.** Dot plots of gene expression (top; blue) and
812 surface protein (bottom; red) expression for populations shown in **A.** where the colour is scaled by
813 mean expression and the dot size is proportional to the percent of the population expressing the
814 gene/protein, respectively. **C.** Bar plot of the mean proportion of cell types shown in **A.** separated
815 by severity status. Stars in key indicate significance (Kruskal-Wallis; * $P < 0.05$, ** $P < 0.01$, *** P
816 < 0.001), arrows represent if proportional change is up or down and colour represents COVID-19
817 severity state. **D.** Bar plot showing the mean proportion of plasmablast and plasma cells expressing
818 IgA, IgD, IgE, IgG or IgM, based on V(D)J information, separated by severity status. **E.** Co-
819 ordinated changes between Tfh and B cells assessed by differential correlation analysis (empirical
820 $P \leq 0.05$). Shown is the Pearson correlation (+/- bootstrap standard error) between Tfh proportions
821 and plasmablast or plasma cell (combined) according to disease severity (only significant trends
822 are shown). **F.** GSEA of pathways from MSigDB hallmark signatures in naive B cells, switched
823 memory B cells and plasmablast for asymptomatic/symptomatic COVID versus healthy. Size of
824 circles indicate (absolute) normalised enrichment score (NES) and colours indicate the severity
825 status. Pathways were considered statistically significant if $P < 0.05$ and FDR < 0.25 (denoted by
826 coloured dots outside the middle grey zone). EMT, Epithelial-mesenchymal transition. **G.** Dot
827 plots representing the expression of genes coding for TNF signalling molecules, activating and
828 inhibitory BCR signaling molecules in naive B cells, switched memory B cells and plasmablast
829 separated by severity status in the rows. Size of circles indicate percent of cells expressing the gene
830 and increasing colour gradient from blue to white to red corresponds to increasing mean expression
831 value (scaled from zero to one across status per gene). **H.** Scatter plot of clonotype size by node
832 closeness centrality gini indices. Each dot represents the gini indices of an individual coloured by
833 severity status. Gini indices were computed for all clonotypes on the x-axis and for clonotypes
834 with > 1 cell on the y-axis (see methods for details). Marginal histograms indicate the distribution

835 of samples in a given severity status along the axes. **I.** BCR overlap incidence plot. Nodes in the
836 inner ring represent individual donors/patients, coloured by severity status, and edges indicate if
837 at least 1 clonotype is shared between two individuals (at least 1 cell in each individual displays
838 an identical combination of heavy and light chain V- and J- gene usage with allowance for somatic
839 hypermutation at the CDR3 junctional region). Nodes in the outer ring indicate the site from which
840 samples were collected (solid grey: Cambridge; grey outline: Sanger; unmarked: Newcastle) **J.**
841 Clonotype size (left panel) and node closeness centrality gini indices (right panel) separated by
842 gender. Statistical tests were performed with non-parametric Mann-Whitney U test between the
843 gender groups within each severity status and were considered statistically significant if
844 Benjamini-Hochberg corrected $P < 0.05$ (denoted by *; n.s. denotes not significant). Colour of
845 asterisks indicates which gender group displays a higher mean gini index (yellow: female; grey:
846 male).

847

848 **Figure 5: Integrated framework of mononuclear cell immune response in blood**

849 Schematic illustration of study highlights. Created with Biorender.com. BCR, B cell receptor; EM,
850 effector memory; TE, terminal effector; Tfh, T follicular helper; Th, T helper; T reg, regulatory T
851 cell

852

853 **Extended Data 1**

854 **A.** Scatter plot displaying the total number of gene counts per sample from each site. **B.** UMAPs
855 from **Fig. 1B** coloured by site. **C.** Boxplot of kBET results calculated both before and after batch
856 correction with Harmony for each cluster in **Fig. 1B** kBET statistic calculating using patient ID as
857 the batch factor. **D.** Dot plots of 5' gene expression (top; blue) and surface protein (bottom; red)
858 expression for populations shown in **Fig. 1A** where the colour is scaled by mean expression and
859 the dot size is proportional to the percent of the population expressing the gene/protein,
860 respectively. **E.** Tile plot showing percentage concordance between COVID-19 PBMC annotation
861 (y-axis) and Azimuth annotation (x-axis) (<https://satijalab.org/azimuth/>).

862

863 **Extended Data 2**

864 **A.** Volcano plots showing results of differential abundance testing. Hypothesis testing was
865 performed using quasi-likelihood F-test comparing healthy controls to cases for linear trends

866 across disease severity groups (healthy > asymptomatic > mild > moderate > severe > critical).
867 Differentially abundant cell types were determined using a 10% false discovery rate (FDR) and
868 marked (*). Hypothesis testing was performed using quasi-likelihood F-test comparing healthy
869 controls to cases. Differentially abundant cell types were determined using a 10% false discovery
870 rate (FDR). **B.** Box and whisker plots showing blood counts for Newcastle data grouped by
871 severity status. Dotted lines and green area mark the normal ranges for each. Kruskal-Wallis with
872 Dunn's post hoc; * $P < 0.05$, ** $P < 0.01$. **C.** Forest plot showing the standard deviation of each
873 clinical/technical factor estimated by the Poisson generalised linear mixed model. The error bars
874 show the standard error estimated from the Fisher information matrix (see **Supplementary Note**
875 **1** for more details). SD, standard deviation. **D.** Box plots displaying the duration of COVID-19
876 symptoms from the onset grouped by severity status. **E.** Volcano plots showing results of
877 differential abundance testing according to time since symptom onset. Differentially abundant
878 (FDR 10%) points are shown in red and labelled by cell type as in **Figure 1A**. **F.** Correlated log
879 fold-changes of cell type abundance changes as a function of symptom duration with (x-axis) and
880 without critically ill patients (y-axis). **G.** Heat map displaying fold change over healthy (left) and
881 dot plot of gene expression where the colour is scaled by mean expression and the dot size is
882 proportional to the percent of the population expressing the gene (right) for genes associated with
883 COVID-19 identified in a recent GWAS study^{25,26} for the cell populations in **Fig. 1B**. **H.** Heat map
884 displaying normalised values of cytokine, chemokine and growth factors in serum of patients with
885 COVID-19.

886

887 **Extended Data 3**

888 **A.** Dot plots of gene expression of C1 complement components for cells in **Fig. 1B** where the
889 colour is scaled by mean expression and the dot size is proportional to the percent of the population
890 expressing the gene. **B.** Dot plots of gene expression of a recently published BAL dataset
891 (accession number GSE145926²⁹) for genes in **Fig. 2A** where the colour is scaled by mean
892 expression and the dot size is proportional to the percent of the population expressing the gene. **C.**
893 Heatmap of differentially expressed genes between megakaryocyte, myeloid and erythroid
894 progenitor clusters. MK, megakaryocyte; My, myeloid. **D.** Bar charts displaying enrichment of an
895 erythroid signature (top) and a myeloid signature (bottom) found in CD34⁻CD38⁻ (left) and
896 CD34⁺CD38⁺ HSPCs (right), separated by severity.

897

898 **Extended Data 4**

899 **A.** UMAP visualisation of T cells separated by sources of donors. **B.** UMAP visualisation
900 showing 2-dimensional kernel density estimates of each T cell type in UMAP space. **C.-E.**
901 UMAP visualisation of T cells coloured by gender (**C.**), disease severity status (**D.**) and age (**E.**).

902

903 **Extended Data 5**

904 **A.** Box plots showing the proportion of cell types shown in **Fig. 3A** separated by severity status.
905 **B.** Volcano plots showing results of differential abundance testing. Cell type abundance counts
906 were modelled either comparing healthy vs. COVID-19 case, or as a function of disease severity.
907 Hypothesis testing was performed using quasi-likelihood F-test comparing healthy controls to
908 cases, or for either a linear or quadratic trend across disease severity groups (asymptomatic > mild
909 > moderate > severe > critical). Differentially abundant cell types were determined using a 10%
910 false discovery rate (FDR). **C.** Gene set enrichment (MSigDB Hallmark 2020) in each T cell type
911 based on differential gene expression (DGE) analysis was performed across COVID-19 disease
912 severity groups, ordered from healthy > asymptomatic > mild > moderate > severe > critical.
913 Statistically significant DE genes were defined with $FDR < 0.01$. Significant enrichments were
914 defined with 10% FDR. **D.** Bar plots showing percent (mean +/- SEM) of CD3⁺CD4⁺ (blue) and
915 CD3⁺CD8⁺ (green) T cells expressing CD107a (left) and CD137 (right) in response to SARS-CoV-
916 2 S peptide stimulation. Significance determined using Kruskal-Wallis with Dunn's post-hoc; * P
917 < 0.05, ** P < 0.01. **E.** Box plots showing clone size distribution for each T cell subset separated
918 by severity status. **F.** Box plots showing clonal diversity for each T cell subset separated by severity
919 status.

920

921 **Extended Data 6**

922 **A.** Heatmap of mean gene set enrichment scores of (top) adult peripheral blood B cell signatures³⁸
923 and (bottom) Human cell atlas bone marrow B cell signatures⁵⁴. Enrichment scores were calculated
924 using *scanpy*'s *tl.score_genes* function, tabulated as the mean of each cell type. Row enrichment
925 value is scaled from 0 to 1 and presented as an increasing gradient from purple, blue, green to
926 yellow which corresponds to increasing mean enrichment score. **B.** (Top) Kruskal-Wallis test
927 results with Benjamini-Hochberg false discovery correction for cell type proportion differences in

928 plasmablast and plasma cells between severity statuses. Significance is denoted by $*P < 0.05$; $**P$
929 < 0.01 ; $***P < 0.001$. (Bottom) Cell type abundance counts were modelled as a function of disease
930 severity. Hypothesis testing was performed using quasi-likelihood F-test comparing asymptomatic
931 to symptomatic covid, for either a linear or quadratic trend across disease severity groups
932 (asymptomatic > mild > moderate > severe > critical). Differentially abundant cell types were
933 determined using a 10% false discovery rate (FDR). **C.** GSEA of pathways from MSigDB v7.2
934 hallmark signatures in immature B cells, non-switched memory B cells, `exhausted` B cells and
935 plasma cells for asymptomatic/symptomatic COVID versus healthy. Size of circles indicate
936 (absolute) normalised enrichment score (NES) and colours indicates the severity status. Pathways
937 were considered statistically significant if $P < 0.05$ and $FDR < 0.25$ (denoted by coloured dots
938 outside the middle grey zone). EMT, Epithelial-mesenchymal transition. **D.** Dot plots of TNF
939 signalling molecules, activating and inhibitory BCR signaling molecules (5' gene expression data)
940 in immature B cells, non-switched memory B cells, `exhausted` B cells and plasma cells separated
941 by severity status in the rows. Size of circles indicate percent of cells expressing the gene and
942 increasing colour gradient from blue to white to red corresponds to increasing mean expression
943 value (scaled from zero to one across status per gene).

944

945 **Extended Data 7**

946 **A.** Single-cell BCR network plots for each severity status coloured by heavy chain isotype class
947 (IgM, IgD, IgA, IgE, or IgG). Each circle/node corresponds to a single B cell with a corresponding
948 set of BCR(s). Each clonotype is presented as a minimally connected graph with edge widths
949 scaled to $1/d+1$ for edge weight d where d corresponds to the total (Levenshtein) edit distance of
950 BCRs between two cells. Size of nodes is scaled according to increasing node closeness centrality
951 scores i.e. nodes that are highly central to a clonotype network will be larger. **B.** (Left) Scatter plot
952 of clonotype/cluster size by vertex size gini indices computed from contracted BCR networks
953 (identical nodes are merged and counted). Each dot represents the gini indices of an individual
954 coloured by severity status. Gini indices were computed for all clonotypes on both x- y-axes (see
955 methods for details). Marginal histograms indicate the distribution of samples in a given severity
956 status along the axes. (Right, top) Cluster/clonotype size (contracted network) gini indices
957 separated by gender. (Right, bottom) Vertex size (contracted network) gini indices separated by
958 gender. Statistical tests were performed with non-parametric Mann-Whitney U test between the

959 gender groups within each severity status and were considered statistically significant if
960 Benjamini-Hochberg corrected $P < 0.05$ (denoted by *; n.s. denotes not significant). Colour of
961 asterisks indicates which gender group display a higher mean gini index (yellow: female; grey:
962 male).

963

964 **Extended Data 8**

965 **A.** UMAP visualisation of B cell lineage and coloured by clonotype size in the V(D)J data. Only
966 expanded clonotypes are coloured (clonotype size > 2). **B.** Single-cell BCR network plots for each
967 severity status coloured by assigned cell type. **C.** Single-cell BCR network plots for each severity
968 status coloured by heavy chain isotype subclass (IgM, IgD, IgA1, IgA2, IgE, IgG1, IgG2, IgG3 or
969 IgG4). Each circle/node corresponds to a single B cell with a corresponding set of BCR(s). Each
970 clonotype is presented as a minimally connected graph with edge widths scaled to $1/d+1$ for edge
971 weight d where d corresponds to the total (Levenshtein) edit distance of BCRs between two cells.
972 Size of nodes is scaled according to increasing node closeness centrality scores i.e. nodes that are
973 highly central to a clonotype network will be larger.

974 **Supplementary Information Guide**

975

976 **Supplementary Table 1:** Patient metadata. Status summary is based on the WHO COVID-19
977 classification (WHO reference number: WHO/2019-nCoV/clinical/2020.5;
978 <https://www.who.int/publications/i/item/clinical-management-of-covid-19>). NA, not applicable.
979 Not-known listed where information was unavailable. O2, supplemental oxygen via nasal
980 cannulae, face mask or non-rebreathe mask. NIV, non-invasive ventilation under continuous
981 (CPAP) or bi-level (BiPAP) positive airways pressure.

982

983 **Supplementary Table 2: CITE-seq panel.** List of Total-seq C antibodies, including clone and
984 barcode.

985

986 **Supplementary Table 3:** Clinical whole blood counts for Newcastle samples. Number of cells x
987 10⁹/L of blood. WBC, white blood cells.

988

989 **Supplementary Table 4:** Concentration in pg/mL of 45 analytes measured in serum. <=0, below
990 the limit of detection; * indicates anti-inflammatory cytokines.

991

992 **Supplementary Note 1:** Further information detailing the poisson linear mixed model for cell type
993 composition analysis.

994

995 **Supplementary Note 2:** List of collaborators and their affiliations from the CITIID-NIHR
996 COVID-19 BioResource.

997

998

999

1000

1001 **Methods**

1002

1003 **Ethics and sample collection:**

1004 *Newcastle:*

1005 Patients were consented under the Newcastle Biobank (REC 17/NE/0361, IRAS 233551) study
1006 and ethical governance. For the COVID-19 positive samples and healthy controls, peripheral blood
1007 was collected in EDTA tubes and serum separator tubes and processed within 4 h of collection.

1008

1009 For the IV-LPS control samples: Ethical approval was granted by a REC (17/YH/0021). Healthy
1010 volunteers gave informed, written consent. LPS was obtained from Clinical Center Reference
1011 Endotoxin (Lots 94332B1 donated by National Institute of Health, Bethesda, Maryland, USA) and
1012 injected intravenously as a bolus dose of 2 ng/kg. Blood samples were taken prior to IV LPS
1013 administration (baseline) and at 90 min, and 10 h post challenge. Venous blood was drawn from
1014 an 18g venous cannula and was collected into EDTA and serum separator tubes. Only samples
1015 from 90 min and 10 h were analysed in this study.

1016

1017 *Cambridge:*

1018 Study participants were recruited between 31/3/2020 and 20/7/2020 from patients attending
1019 Addenbrooke's Hospital with a suspected or nucleic acid amplification test (NAAT) confirmed
1020 diagnosis of COVID-19 (including point of care testing (Collier et al., 2020; Mlcochova et al.,
1021 2020)), patients admitted to Royal Papworth Hospital NHS Foundation Trust or Cambridge and
1022 Peterborough Foundation Trust with a confirmed diagnosis of COVID-19, together with Health
1023 Care Workers identified through staff screening as PCR positive for SARS-CoV-2 (Rivett et al.,
1024 2020). Controls were recruited among hospital staff attending Addenbrooke's serology screening
1025 programme, and selected to cover the whole age spectrum of COVID-19 positive study
1026 participants, across both genders. Only controls with negative serology results (45 out of 47) were
1027 subsequently included in the study. Recruitment of inpatients at Addenbrooke's Hospital and
1028 Health Care Workers was undertaken by the NIHR Cambridge Clinical Research Facility outreach
1029 team and the NIHR BioResource research nurse team. Ethical approval was obtained from the East
1030 of England – Cambridge Central Research Ethics Committee ("NIHR BioResource" REC ref
1031 17/EE/0025, and "Genetic variation AND Altered Leukocyte Function in health and disease -

1032 GANDALF” REC ref 08/H0308/176). All participants provided informed consent. Each
1033 participant provided 27 mL of peripheral venous blood collected into a 9 mL sodium citrate tube.

1034

1035 *UCL/Sanger:*

1036 Subjects 18 years and older were included from two large hospital sites in London, United
1037 Kingdom, namely University College London Hospitals NHS Foundation Trust and Royal Free
1038 London NHS Foundation Trust during the height of the pandemic in the United Kingdom (April
1039 to July 2020). Ethical approval was given through the Living Airway Biobank, administered
1040 through UCL Great Ormond Street Institute of Child Health (REC reference: 19/NW/0171, IRAS
1041 project ID 261511), as well as by the local R&D departments at both hospitals. At daily virtual
1042 COVID-19 co-ordination meetings suitable patients were chosen from a list of newly diagnosed
1043 and admitted patients within the preceding 24 h (based on a positive nasopharyngeal swab for
1044 SARS-CoV-2). Patients with typical clinical and radiological COVID-19 features but with a
1045 negative screening test for SARS-CoV-2 were excluded. Other excluding criteria included active
1046 haematological malignancy or cancer, known immunodeficiencies, sepsis from any cause and
1047 blood transfusion within 4 weeks. Maximal severity of COVID-19 was determined retrospectively
1048 by determining the presence of symptoms, the need of oxygen supplementation and the level of
1049 respiratory support. Peripheral blood sampling was performed prior to inclusion to any
1050 pharmacological interventional trials.

1051

1052 Samples were collected and transferred to a Category Level 3 facility at University College London
1053 and processed within 2 h of sample collection. Peripheral blood was centrifuged after adding Ficoll
1054 Paque Plus and PBMCs, serum and neutrophils separated, collected and frozen for later processing.

1055

1056 **Clinical status assignment**

1057 Clinical metadata was collected at the point of sample collection, including current oxygen
1058 requirements and location. This was used to assign disease severity status. Patients based on a
1059 ward and not requiring oxygen were defined as “Mild”. Patients outside of an intensive care unit
1060 (ICU) environment requiring oxygen were defined as “Moderate”. All patients on ICU and/or
1061 requiring non-invasive ventilation were defined as “Severe”. Patients requiring intubation and

1062 ventilation were defined as “Critical”. There were no patients in ICU that did not require
1063 supplemental oxygen.

1064

1065 **PBMC isolation and dead cell removal:**

1066 *Newcastle:*

1067 PBMCs were isolated from blood samples using Lymphoprep (StemCell Technologies) density
1068 gradient centrifugation as per manufacturer’s instructions. Single cell suspensions were then
1069 washed with Dulbecco’s phosphate buffered saline (PBS) (Sigma) and frozen in 5-10 million cell
1070 aliquots in 90% (v/v) heat inactivated fetal calf serum (FCS) (Gibco) 10% (v/v) DMSO (Sigma
1071 Aldrich). On the day of the experiment the cells were thawed for 1 min, transferred to Wash buffer
1072 (PBS supplemented with 2% (v/v) FCS and 2 mM EDTA), and centrifuged at 500 g for 5 min.
1073 Resuspended cells were passed through a 30 µm filter and counted prior to live cell MACS
1074 enrichment with the Dead cell removal kit (Miltenyi Biotec) as per manufacturer’s instructions.
1075 Cell pellets were resuspended in microbeads and incubated at room temperature for 15 min. Each
1076 stained sample was passed through an LS column (Miltenyi Biotec) and rinsed with Binding buffer
1077 (Miltenyi Biotec) before centrifugation. Cell pellets were resuspended in Wash buffer and counted
1078 for CITE-seq antibody staining.

1079

1080 *Cambridge:*

1081 Peripheral blood mononuclear cells (PBMCs) were isolated using Leucosep tubes (Greiner Bio-
1082 One) with Histopaque 1077 (Sigma) by centrifugation at 800 g for 15 min at room temperature.
1083 PBMCs at the interface were collected, rinsed twice with autoMACS running buffer (Miltenyi
1084 Biotec) and cryopreserved in FBS with 10% DMSO. All samples were processed within 4 h of
1085 collection. Purified PBMCs were thawed at 37°C, transferred to a 50 mL tube and 10 volumes of
1086 pre-warmed thawing media (IMDM (Gibco 12440-053) with 50% (v/v) FCS (not heat inactivated;
1087 Panbiotech P40-37500) and 0.1 mg/mL DNaseI (Worthington LS002139)) were added slowly and
1088 dropwise, followed by centrifugation at 500 g for 5 min. The pellet was resuspended in 1 mL of
1089 FACS buffer (PBS (Sigma D8537) with 3% (v/v) heat-inactivated FCS) and viability of each
1090 sample was assessed by counting in an improved Neubauer chamber using Trypan blue. Pools of
1091 4 samples were generated by combining 0.5 million live cells per individual (2 million live cells
1092 total). The pools were washed twice in FACS buffer (10 mL and 2 mL, respectively) followed by

1093 centrifugation for 5 min at 500 g. The pellet was then resuspended in 35 μ L of FACS buffer and
1094 the viability of each pool was assessed.

1095

1096 *UCL/Sanger:*

1097 Peripheral whole blood was collected in EDTA tubes and processed fresh via Ficoll-Paque Plus
1098 separation (GE healthcare,17144002). The blood was first diluted with 5 mL 2 mM EDTA-PBS
1099 (Invitrogen, 1555785-038), before 10-20 mL of diluted blood was carefully layered onto 15 mL of
1100 Ficoll in a 50 mL falcon tube. If the sample volume was less than 5 mL, blood was diluted with an
1101 equal volume of EDTA-PBS and layered onto 3 mL Ficoll. The sample was centrifuged at 800 g
1102 for 20 min at room temperature. The plasma layer was carefully removed and the peripheral blood
1103 mononuclear cell (PBMC) layer collected using sterile Pasteur pipette. The PBMC layer was
1104 washed with 3 volumes of EDTA-PBS by centrifugation at 500 g for 10 min. The pellet was
1105 suspended in EDTA-PBS and centrifuged again at 300 g for 5 min. The PBMC pellet was collected
1106 and the cell number and viability assessed using Trypan blue. Cell freezing medium (90% FBS,
1107 10% DMSO) was added dropwise to PBMCs slowly on ice and the mixture cryopreserved at -
1108 80°C until further full sample processing.

1109

1110 **Total-seq C antibody staining and 10x Chromium loading**

1111 *Newcastle:*

1112 200,000 cells from each donor were stained with Human TruStain FcX™ Fc Blocking Reagent
1113 (Biolegend 422302) for 10 min at room temperature. The cells were then stained with the custom
1114 panel Total-seq C (Biolegend 99813; see **Supplementary Table 2**) for 30 min at 4°C. Cells were
1115 then washed twice with PBS supplemented with 2% (v/v) FCS and 2 mM EDTA (Sigma) before
1116 resuspending in PBS and counting. 20,000-30,000 cells per sample were loaded onto the 10x
1117 Chromium controller using Chromium NextGEM Single Cell V(D)J Reagent kits v1.1 with
1118 Feature Barcoding technology for Cell Surface Protein (10x Genomics) according to the
1119 manufacturer's protocol.

1120

1121 *Cambridge:*

1122 Half a million viable cells were resuspended in 25 μ L of FACS buffer and incubated with 2.5 μ L
1123 of Human TruStain FcX™ Fc Blocking Reagent (BioLegend 422302) for 10 min at 4°C. The

1124 TotalSeq-C™ antibody cocktail (BioLegend 99813; see **Supplementary Table 2**) was centrifuged
1125 at 14,000 g at 4°C for 1 min, resuspended in 52 µL of FACS buffer, incubated at room temperature
1126 for 5 min and centrifuged at 14,000 g at 4°C for 10 min. 25 µL were subsequently added to each
1127 sample pool and incubated for 30 min at 4°C in the dark. Pools were washed 3 times with 27
1128 volumes (1.4 mL) of FACS buffer, followed by centrifugation at 500 g for 5 min. The pellet was
1129 resuspended in 62.5 µL of 1 x PBS + 0.04% BSA (Ambion, #AM2616), filtered through a 40 µm
1130 cell strainer (Flowmi, H13680-0040) and viable cells of each sample pool were counted in an
1131 improved Neubauer chamber using Trypan blue. 50,000 live cells (up to a maximum of 60,000
1132 total cells) for each pool were processed using Single Cell V(D)J 5' version 1.1 (1000020) together
1133 with Single Cell 5' Feature Barcode library kit (1000080), Single Cell V(D)J Enrichment Kit,
1134 Human B Cells (1000016) and Single Cell V(D)J Enrichment Kit, Human T Cells (1000005) (10x
1135 Genomics) according to the manufacturer's protocols.

1136

1137 *UCL/Sanger:*

1138 Frozen PBMC samples were thawed quickly in a water bath at 37°C. Warm RPMI1640 medium
1139 (20-30 mL) containing 10% FBS was added slowly to the cells before centrifuging at 300 g for 5
1140 min, the pellet was then washed with 5 mL RPMI1640-FBS and centrifuged again (300 g for 5
1141 min). The PBMC pellet was collected and cell number and viability determined using Trypan blue.
1142 PBMCs from four different donors were then pooled together at equal numbers (1.25×10^5 PBMCs
1143 from each donor) to make up 5.0×10^5 cells in total. The remaining cells were used for DNA
1144 extraction (Qiagen, 69504). The pooled PBMCs were stained with TotalSeq-C antibodies
1145 (Biolegend, 99814) according to manufacturer's instructions. After incubating with 0.5 vial of
1146 TotalSeq-C for 30 min at 4°C, PBMCs were washed three times by centrifugation at 500 g for 5
1147 min at 4°C. PBMCs were counted again and processed immediately for 10x 5' single cell capture
1148 (Chromium Next GEM Single Cell V(D)J Reagent Kit v1.1 with Feature Barcoding technology
1149 for cell Surface Protein-Rev D protocol). Two lanes of 25,000 cells were loaded per pool on a 10x
1150 chip.

1151

1152

1153

1154

1155 **Library preparation and sequencing**

1156 *Newcastle and UCL/Sanger:*

1157 Gene expression, TCR enriched and BCR enriched libraries were prepared for each sample
1158 according to the manufacturer's protocol (10x Genomics). Cell surface protein libraries were
1159 subjected to double the manufacturer's recommended primer concentration and 7-8 amplification
1160 cycles during the sample index PCR to reduce the likelihood of daisy chains forming. Libraries
1161 were pooled per patient using the following ratio 6:2:1:1 for gene expression, cell surface
1162 protein, TCR enriched and BCR enriched libraries. All libraries were sequenced using a
1163 NovaSeq 6000 (Illumina) to achieve a minimum of 50,000 paired end reads per cell for gene
1164 expression and 20,000 paired end reads per cell for cell surface protein, TCR enriched and BCR
1165 enriched.

1166

1167 *Cambridge:*

1168 The samples were subjected to 12 cycles of cDNA amplification and 8 cycles for the cell surface
1169 protein library construction. Following this, the libraries were processed according to the
1170 manufacturer's protocol. Libraries were pooled per sample using a ratio 9:2.4:1:0.6 for gene
1171 expression, cell surface, TCR enriched and BCR enriched libraries. Samples were sequenced using
1172 a NovaSeq 6000 (Illumina), using S1 flowcells.

1173

1174 **Alignment and quantification**

1175 Droplet libraries were processed using Cellranger v4.0. Reads were aligned to the GRCh38 human
1176 genome concatenated to the SARS-Cov-2 genome (NCBI SARS-CoV-2 isolate Wuhan-Hu-1)
1177 using STAR⁵⁵ and unique molecular identifiers (UMIs) deduplicated. CITE-seq UMIs were
1178 counted for GEX and ADT libraries simultaneously to generate feature X droplet UMI count
1179 matrices.

1180

1181 **Doublet identification**

1182 *Newcastle:*

1183 *Scrublet* (v0.2.1) was applied to each sample to generate a doublet score. These formed a bimodal
1184 distribution so the tool's automatic threshold was applied.

1185

1186 *Cambridge:*

1187 Non-empty droplets were called within each multiplexed pool of donors using the *emptyDrops*
1188 function implemented in the Bioconductor package *DropletUtils*, using a UMI threshold of 100
1189 and FDR of 1%. The probability of being a doublet was estimated for each cell per sample (that is
1190 one 10x lane) using the “*doubletCells*” function in *scrnan* based on highly variable genes (HVGs).
1191 Next, we used “*cluster_walktrap*” on the SNN-Graph that was computed on HVGs to form highly
1192 resolved clusters per sample. Per-sample clusters with either a median doublet score greater than
1193 the median + 2.5 x MAD or clusters containing more than the median + 2.5 MAD genotype
1194 doublets were tagged as doublets. This was followed by a second round of highly-resolved
1195 clustering across the whole data set, in which again cells belonging to clusters with a high
1196 proportion (> 60%) of cells previously labelled as doublets were also defined as doublets.

1197

1198 *UCL/Sanger:*

1199 For pooled donor CITE-seq samples, the donor ID of each cell was determined by genotype-based
1200 demultiplexing using *souporcell* version 2⁵⁶. *Souporcell* analyses were performed with
1201 ‘skip_remap’ enabled and a set of known donor genotypes given under the ‘common_variants’
1202 parameter. The donor ID of each souporcell genotype cluster was annotated by comparing each
1203 souporcell genotype to the set of known genotypes. Droplets that contained more than one
1204 genotype according to souporcell were flagged as ‘ground-truth’ doublets for heterotypic doublet
1205 identification. Ground-truth doublets were used by *DoubletFinder* 2.0.3⁵⁷ to empirically determine
1206 an optimal ‘pK’ value for doublet detection. *DoubletFinder* analysis was performed on each
1207 sample separately using 10 principal components, a ‘pN’ value of 0.25, and the ‘nExp’ parameter
1208 estimated from the fraction of ground-truth doublets and the number of pooled donors.

1209

1210 **CITE-seq background signal removal**

1211 Background antibody- and non-specific staining was subtracted from ADT counts in each data set
1212 from the 3 data acquisition sites separately. ADT counts for each protein were first normalised
1213 using counts per million (CPM) and log transformed, with a +1 pseudocount. To estimate the
1214 background signal for each protein, a 2-component gaussian mixture model (GMM), implemented
1215 in the *mclust* R package function *Mclust*, was fit across the droplets with a total UMI count > 10
1216 and < 100 from each experimental sample separately. The mean of the first GMM component for

1217 each protein was then subtracted from the log CPM from the QC-passed droplets in the respective
1218 experimental sample.

1219

1220 **Quality control, normalisation, embedding and clustering**

1221 Combined raw data from the three centres was filtered to remove those that expressed fewer than
1222 200 genes and >10% mitochondrial reads. Data was normalised (scanpy: *normalize_total*), log+1
1223 corrected (scanpy: *log1p*) and highly variable genes identified using the Seurat vst algorithm
1224 (scanpy: *highly_variable_genes*). Harmony was used to adjust principal components by sample ID
1225 and used to generate the neighbourhood graph and embedded using UMAP. Clustering was
1226 performed using the Leiden algorithm with an initial resolution of 3. For initial clustering,
1227 differentially expressed genes were calculated using Wilcoxon rank-sum test.

1228

1229 **Cluster differential abundance testing**

1230 Numbers of cells of each cell subtype were quantified in each patient and control sample (donors)
1231 to compute a cell type X donor counts matrix. Cell type abundance counts were modelled as a
1232 function of either disease severity or days from symptom onset, adjusting for age, gender and
1233 batch, in a NB GLM, implemented in the Bioconductor package *edgeR*. Counts were normalised
1234 in the model using the (log) of the total numbers of all cells captured for each donor. Hypothesis
1235 testing was performed using quasi-likelihood F-test for either a linear or quadratic trend across
1236 disease severity groups (asymptomatic > mild > moderate > severe > critical), or comparing
1237 healthy controls to SARS-CoV-2 infected donors (healthy vs. all asymptomatic, mild, moderate,
1238 severe & critical). Differentially abundant cell types were determined using a 10% false discovery
1239 rate (FDR). Due to compositional differences across sites, when analysing differential abundance
1240 of myeloid populations (figure 2), only samples from Ncl and UCL/Sanger were included.

1241

1242 **Relative importance of metadata on cell type composition**

1243 The number of cells for each sample ($N=110$ samples in total with complete metadata) and cell
1244 type (18 different cell types in total) combination was modelled with a generalised linear mixed
1245 model with a Poisson outcome. The 5 clinical factors (COVID-19 swab result, age, sex, disease
1246 severity at day 0 and days from onset) and the 2 technical factors (patient and sequencing centre)
1247 were fitted as random effects to overcome the collinearity among the factors. The effect of each

1248 clinical/technical factor on cell type composition was estimated by the interaction term with the
1249 cell type (see **Supplementary Note 1** for detail). The likelihood ratio test was performed to assess
1250 the statistical significance of each factor on cell type abundance by removing one interaction term
1251 from the full model at a time. The number of factors was used to adjust multiple testing with the
1252 Bonferroni approach. The ‘glmer’ function in the *lme4* package implemented on R was used to fit
1253 the model. The standard error of variance parameter for each factor was estimated using the
1254 *numDeriv* package.

1255

1256 **Cydar Analysis**

1257 We utilized cydar to identify changes in cell composition across the different severity groups based
1258 on the protein data alone. First, the background-corrected protein counts from the three different
1259 sites were integrated using the ‘fastMNN’ method ($k = 20$, $d = 50$, $\text{cos.norm} = \text{TRUE}$) in *scraper*⁵⁸.
1260 The batch-corrected counts for 188 proteins (4 rat/mouse antibody isotypes were removed) were
1261 then used to construct hyperspheres using the ‘countCells’ function ($\text{downsample} = 8$) with the
1262 tolerance parameter chosen so that each hypersphere has at least 20 cells which was estimated
1263 using the ‘neighborDistances’ function. To assess whether the abundance of cells in each
1264 hypersphere are associated with disease status, hypersphere counts were analyzed using the quasi-
1265 likelihood (QL) method in *edgeR*. After filtering out hyperspheres with an average count per
1266 sample below 5 we fitted a mean-dependent trend to the NB dispersion estimates. The trended
1267 dispersion for each hypersphere was used to fit a NB GLM using the log-transformed total number
1268 of cells as the offset for each sample and blocking for sex, age and batch. The QL F-test was used
1269 to compute P values for each hypersphere which were corrected for multiple testing using the
1270 spatial FDR method in *cydar*.

1271

1272 **Comparisons of PBMC annotation using the Azimuth tool**

1273 The final annotation of PBMCs was compared to a published PBMC annotation using the *Azimuth*
1274 tool (<http://azimuth.satijalab.org/app/azimuth>). Because of size restrictions of 100,000 cells, our
1275 data was subsampled to 10% of the total cells. After running the algorithm, results with a prediction
1276 score < 0.5 were removed (5.8% of total removed). For each cluster in the COVID-19 PBMC data,
1277 the percentage of cells mapped to each cluster in the *Azimuth* annotation was calculated.

1278

1279 **Interferon, TNF and JAK-STAT response scoring**

1280 A list of genes related to response to type I interferons was obtained from the GSEA Molecular
1281 Signatures Database (MSigDB) (GO: 0034340). Enrichment of the interferon score was measured
1282 using the *tl.score_genes* tool in *scanpy* which subtracts the average expression of all genes in the
1283 dataset from the average expression of the genes in this list. The scores were averaged across
1284 clusters and clinical status and expressed as a fold-change over the interferon score in the
1285 equivalent healthy cluster.

1286

1287 **kBET analysis**

1288 The *kBET*⁵⁹ algorithm (<https://github.com/theislab/kBET>) was run for each cluster defined in Fig.
1289 1 using the Uniform manifold and projection (UMAP) coordinates generated from Harmony-
1290 adjusted principal components, and the sample number as the batch factor. The same procedure
1291 was then performed using the same annotation but using the UMAP coordinates generated from
1292 non-Harmony-adjusted principal components. The resultant rejection rates were averaged across
1293 clusters and compared using a Wilcoxon paired signed rank test.

1294

1295 **Bronchoalveolar lavage data analysis**

1296 ScRNAseq data from BAL was obtained from GEO (accession number GSE145926²⁹). Raw data
1297 was analysed using the same pipeline as PBMC data, specifically using the same quality control
1298 cut-offs (min of 200 genes and <10% mitochondrial reads/cell) and batch-corrected using
1299 Harmony by donor ID. To gain greater resolution of mononuclear phagocytes the DC and
1300 macrophages were analysed with further rounds of sub-clustering to identify DC1, DC2 and
1301 mature DC.

1302

1303 **PAGA analysis of blood monocytes and BAL macrophages**

1304 Annotated raw expression datasets of BAL macrophages and COVID-19 PBMCs were merged
1305 and data log-normalised and scaled as for the original datasets. The top 3000 highly variable genes
1306 were chosen using the *Seurat* “vst” method and used for downstream analysis. Principal
1307 components were batch corrected by donor and used to build a neighborhood graph. The PAGA
1308 tool in *scanpy* (*tl.paga*) was used to generate the abstracted graph between clusters.

1309

1310 **CellphoneDB**

1311 *CellphoneDB*⁶⁰ was used to assess putative interactions between monocytes (CD14_mono,
1312 CD83_CD14_mono, C1_CD16_mono, CD16_mono, Prolif_mono) and platelets. The tool was run
1313 for 100 iterations and an expression threshold of 0.25 (limiting the analysis to genes expressed by
1314 25% of cells). For downstream analysis we focused on interactions between platelets and any
1315 monocyte subset.

1316

1317 **HPSC commitment scoring**

1318 HPSCs were subsetted from the data and Leiden clusters generated using the same pipeline and
1319 parameters as for the whole PBMC dataset. Differentially expressed genes between the HSPC
1320 clusters that showed evidence of lineage commitment (MK, Erythroid and Myeloid) were
1321 calculated using *FindAllMarkers* tool in *Seurat* (with thresholds of genes expressed by 25% of
1322 cells and with a log fold-change of 0.25) and genes with an adjusted p-value cut-off of 0.05 were
1323 used to generate gene signatures for each. Enrichment of these signatures in the CD38 negative
1324 and CD38 positive HSPC clusters were calculated using the *tl.score_genes* in *scanpy*. The average
1325 expression of these enrichment scores in the CD38 negative and CD38 positive HSPC clusters was
1326 calculated and normalised to their expression in healthy patients.

1327

1328 **Multiplex cytokine analysis**

1329 Serum was obtained from peripheral blood in red topped serum Vacutainers® (BD, 367815) and
1330 allowed to clot for at least 30 min before centrifugation (800 g for 10 min) to separate the serum.
1331 After collection, serum was frozen at -80°C and thawed on ice on the day of experiment. The assay
1332 was carried out using the Cytokine/Chemokine/Growth Factor 45-Plex Human ProcartaPlex™
1333 Panel 1 kit (Invitrogen, EPX450-12171-901), utilising the Luminex xMAP technology and
1334 according to the manufacturer's protocol. Each sample was run in duplicate. The values of each
1335 analyte were detected using the MAGPIX® system and analysed using the ProcartaPlex Analyst
1336 version 1.0 Software (ThermoFisher Scientific).

1337

1338 **Re-stimulation of PBMC with SARS-Cov-2 peptide S**

1339 Purified PMBC were thawed at 37°C, transferred into a 15 mL tube with 10 mL pre-warmed
1340 complete culture media RPMI-1640 medium (Sigma Aldrich, R0883) supplemented with 10%

1341 (v/v) FCS (Gibco, 10270-106), 1% (v/v) Penicillin/Streptomycin (100 U/mL and 100 µg/mL
1342 respectively; Sigma Aldrich, P0781) and 1% (v/v) L-Glutamine (2 mM; Sigma Aldrich, G7513),
1343 referred as RPMI10, followed by centrifugation at 500 g for 5 min. Cell pellet was resuspended in
1344 500 µL RPMI10 with added DNase (1 µg/mL, Merck, 10104159001), divided into 5 wells of
1345 round bottom 96-well plate and left to rest at 37°C for an hour. Cells were stimulated with SARS-
1346 CoV-2 PepTivator peptide S for pan-HLA (2 µg/mL, Miltenyi Biotech, 136-126-700) and
1347 PMA/Ionomycin as a control (2 µL/mL, Cell Activation cocktail, Biolegend, 423301), and
1348 incubated at 37°C for 2 h. Negative controls were left untreated. Brefeldin A (2 µg/mL, GolgiPlug,
1349 BD Bioscience, 555029) and anti-CD107a-BB700 antibody (1:50, clone H4A3, BD Bioscience,
1350 566558) was added for additional 4 h into all conditions. Cells were stained for detection of
1351 activation induced markers and intracellular cytokines 6 h after stimulation and subjected to flow
1352 cytometry.

1353

1354 **Flow Cytometry of stimulated cells**

1355 PBMC stimulated for 6 h with the SARS-Cov-2 peptide were washed with PBS, and cell surface
1356 stained for 1 h at room temperature: anti-CD14-FITC (1:50, clone M5E2, BD Biosciences,
1357 555397), anti-CD19-FITC (1:50, clone 4G7, BD Biosciences, 345776), anti-CD137-Pe-Dazzle594
1358 (1:50, clone 4B4-1, Biolegend, 309826), anti-CCR7-PE-Cy7 (1:50, clone G043H7, Biolegend,
1359 353226), anti-CD45RO-APC-H7 (1:50, clone UCHL1, BD Biosciences, 561137), anti-CD28-
1360 BV480 (1:50, clone CD28.2, BD Biosciences, 566110), anti-CD4-BV785 (1:100, clone SK3,
1361 Biolegend, 344642), anti-CD3-BUV395 (1:50, clone UCHT1, BD Biosciences, 563546), anti-
1362 CD8-BUV496 (1:100, clone RPA-T8, BD Biosciences, 564804), anti-CD25-BUV737 (1:100,
1363 clone 2A3, BD Biosciences, 612806) and viability dye Zombie Yellow (1:200, Biolegend,
1364 423104). Cells were washed with PBS 2% (v/v) FCS, fixed with 4% (w/v) paraformaldehyde
1365 (ThermoFisher Scientific, 28908) and kept at 4°C overnight. Subsequently, cells were washed with
1366 PBS, permeabilized with Perm/Wash buffer (BD Biosciences, 554723) according manufacturer's
1367 instruction, and stained with intracellular antibodies for 1 h on ice: anti-IL10-PE (1:10, clone
1368 JES3-19F1, BD Biosciences, 559330), anti-IFN-APC (1:25, Miltenyi Biotec, 130-090-762), anti-
1369 TNF-AF700 (1:50, clone MAb11, Biolegend, 502928), anti-IL2-BV421 (1:100, clone 5344.111,
1370 BD Biosciences, 562914), anti-CD154-BV605 (1:50, clone 24-31, Biolegend, 310826). Cells were

1371 washed, transferred to flow cytometry 5 mL tubes, and acquired on Symphony A5 flow cytometer
1372 (BD Biosciences). Data were analysed by FlowJo V10 (BD Biosciences).

1373

1374 **GSEA analysis**

1375 Pre-ranked gene set analysis (prGSEA) on MSigDB v7.2 Hallmark genesets⁶¹ was performed
1376 using pre-ranked gene lists with fgsea⁶² in R. Genes were pre-ranked according to signed $-\log_{10}P$ -
1377 values for all prGSEA procedures. For B cells, generation of rank gene list was performed using
1378 Wilcoxon rank sum test (via *tl.rank_genes_groups* in *scanpy*) with each Day 0 COVID statuses
1379 (asymptomatic to symptomatic critical) as the “tests” versus Day 0 Healthy samples as
1380 “reference/control”.

1381

1382 **T cell clustering, annotation and visualisation**

1383 Droplets labelled as T cells (“CD4”, “CD8”, “Treg”, “MAIT”, “gdT”) were subset from those in
1384 Fig. 1B and re-clustered using a set of HVGs calculated within each batch, the union of which
1385 were used to estimate the first 50 principal components across cells using the *irbla* R package.
1386 Batch effects were removed across the first 30 PCs using the *fastMNN*⁵⁸ implementation in the
1387 Bioconductor package *batchelor* (k=50). A k-nearest neighbour graph (k=20) was computed
1388 across these 30 batch-integrated PCs using the *buildKNNGraph* function implemented in the
1389 Bioconductor package *scrn*, which was then used to group cells into connected communities
1390 using Louvain⁶³ clustering implemented in the R package *igraph*. Clusters that displayed mixed
1391 profiles of T and other lymphoid lineages, i.e. CD19, CD20 and immunoglobulin genes, were
1392 classed as doublets and removed from down-stream analyses. Clusters indicative of NK cells
1393 (CD3⁺CD56⁺) were subsequently annotated as such and removed from T cell analyses. Remaining
1394 clusters were annotated using a combination of canonical protein & mRNA (italicised) markers
1395 for major $\alpha\beta$ T cells (CD4, CD8, CCR7, CD45RA, CD45RO, CD62L, CD27, CD38, CD44,
1396 CXCR5, CD40LG *CCR7*, *FOXP3*, *IKZF2*), $\gamma\delta$ T cells (*V γ 9*, *V γ 2*, *TRGV9*, *TRDV2*) and invariant
1397 T cells; MAIT (*V α 24-J α 18*, *TRAV1.2*), NKT (CD3, CD16, CD56, *NCAM1*, *NCR1*, *FCGR3A*).
1398 Polarized CD4⁺ T cell annotations were refined using the combination of transcription factor genes
1399 and expressed cytokines for the respective helper T cell types: Th1 (*IFNG*, *TBX21*, *TNFA*), Th2
1400 (*GATA3*, *IL4*, *IL5*), Th17 (*RORC*, *IL17A*, *IL17F*, *IL21*). Where clusters appeared heterogeneous in
1401 their expression of T cell lineage markers, single cell annotations were refined based on the co-

1402 expression of specific marker gene and protein pairs. Dot plots to visualise marker protein and
1403 mRNA expression across clusters were generated using the R package *ggplot2*. UMAP⁶⁴ was used
1404 to project all single T cells into a 2D space (k=31) using the first 30 batch-integrated PCs as input
1405 using the R package *umap*.

1406

1407 **T cell differential gene expression analysis**

1408 Differential gene expression (DGE) analysis was performed across COVID-19 disease severity
1409 groups, ordered from healthy > asymptomatic > mild > moderate > severe > critical. Donor
1410 pseudo-bulk samples were first created by aggregating gene counts for each annotated T cell type,
1411 within each donor, where there were at least 20 cells of that type. Genes with fewer than 3 counts
1412 in any given pseudo-bulk, or fewer than 5 counts in total across donor pseudo-bulk samples, were
1413 removed prior to analysis. DGE testing was performed using a negative binomial generalized
1414 linear model (NB GLM) implemented in the Bioconductor package *edgeR*^{65,66}. Statistically
1415 significant DE genes were defined with FDR < 0.1. Functional annotation enrichment was
1416 performed using the Bioconductor package *enrichR*⁶⁷. Up- and down-regulated DE genes in each
1417 T cell type were used as input, testing separately against the MSigDB Hallmark 2020 and
1418 Transcription Factor Protein-Protein Interactions gene sets. Significant enrichments were defined
1419 with 1% FDR.

1420

1421 **T cell receptor analysis**

1422 Single-cell TCRs were computed from the TCR-seq data using Cellranger v4.0.0. The unfiltered
1423 output of reconstructed TCR contigs across all 3 sites (Newcastle, Cambridge, UCL) were
1424 combined prior to filtering using: 1) full length CDR3, 2) droplet barcode matched a T cell droplet,
1425 3) productive CDR3 spanning V+J genes. Chain-specific TCR clones were defined for each
1426 observed α and β chain by first concatenating the V, J and identical CDR3 nucleotide sequences.
1427 For each single T cell, these chains were then combined to form a single clonotype, removing cells
1428 that contained: 1) > 2 β chains and > 2 α chains, 2) a single α or a single β chain only. T cells with
1429 exactly 2 β chains and 1 α chain, or those with exactly 2 α chains and 1 β chain were retained. TCR
1430 clonotypes were counted within each donor sample, and expanded clones were defined where > 1
1431 cell was assigned to the TCR clonotype.

1432

1433 The proportion of expanded clones as a function of a linear trend across disease severity groups
1434 was modelled using logistic regression, adjusted for age, gender and batch. A separate model was
1435 run for each T cell subtype which contained at least 5 cells assigned to the expanded TCR
1436 clonotypes. Linear trend p-values were corrected for multiple testing using the Benjamini &
1437 Hochberg procedure⁶⁸.

1438
1439 The TE:EM ratio was calculated within each donor, using the number of observed expanded
1440 clonotypes. The TE:EM ratio change across COVID-19 severity was tested using a robust linear
1441 model implemented in the R package *robustbase*, regressing TE:EM ratio on disease severity as
1442 an ordered linear variable (asymptomatic > mild > moderate > severe > critical), adjusted for age,
1443 gender and batch. Statistical significance was defined based on the linear trend across disease
1444 severity ($p \leq 0.01$).

1445
1446 **Differential correlation analysis**

1447 Changes in the correlations between PBMC cell types were computed using a differential
1448 correlation analysis, implemented in the R package *DCARS*⁶⁹. Cell type proportions were
1449 computed by normalizing the counts of each cell type within each donor by the total number of
1450 cells captured for that donor sample. Donor samples were ranked according to their disease
1451 severity (healthy > asymptomatic > mild > moderate > severe > critical). Differential correlation
1452 analysis was then performed between CD4.Tfh vs all B cell types. Statistically significant
1453 differentially correlated cell types were defined with empirical p-value ≤ 0.05 , estimated from
1454 10,000 permutations.

1455
1456 **BCR V(D)J analysis**

1457 Single-cell V(D)J data from the 5' Chromium 10x kit were initially processed with *cellranger-vdj*
1458 (4.0.0). BCR contigs contained in *filtered_contigs.fasta* and *filtered_contig_annotations.csv* from
1459 all three sites were then pre-processed using *immcantion* inspired preprocessing pipeline⁷⁰
1460 implemented in the *dandelion* python package; *dandelion* is a novel single cell BCR-seq analysis
1461 package for 10x Chromium 5' data. All steps outlined below are performed using *dandelion*
1462 v0.0.26 and is available at <https://github.com/zktuong/dandelion>.

1463

1464 **BCR preprocessing**

1465 Individual BCR contigs were re-annotated with *igblastn* v1.1.15 using the IMGT reference
1466 database (date downloaded: 30-June-2020)⁷¹ by calling *changeo*'s *AssignGenes.py* script and re-
1467 annotated contigs in *blast* format were parsed into the Adaptive Immune Receptor Repertoire
1468 (AIRR) standards 1.3 format with *changeo*'s *MakeDB.py* script. Amino acid sequence alignment
1469 information not present in the output from *blast* format were retrieved from re-annotation with
1470 *igblastn* in *airr* format. Heavy chain V-gene alleles were corrected for individual genotypes with
1471 TIgGER⁷² (v1.0.0) using a modified *tigger-genotype.R* script from *immcantation* suite. Germline
1472 sequences were reconstructed based on the genotype corrected V-gene assignments using
1473 *changeo*'s (v1.0.1) *CreateGermines.py* script; contigs which fail germline sequence reconstruction
1474 were removed from further analysis. Constant genes were re-annotated using *blastn* (v2.10.0+)
1475 with CH1 regions of constant gene sequences from IMGT followed by pairwise alignment against
1476 curated sequences to correct assignment errors due to insufficient length of constant regions.

1477

1478 **BCR filtering**

1479 Contigs assigned to cells that passed quality control on the transcriptome data were retained for
1480 further quality control assessment, which includes checks for: i) contigs with mismatched locus,
1481 V-, J- and constant gene assignments were removed from the analysis; ii) cell barcodes with
1482 multiple heavy chain contigs were flagged for filtering. Exceptions to this would be when a) the
1483 multiple heavy chain contigs were assessed to have identical V(D)J sequences but assigned as
1484 different contigs belonging to the same cell by *cellranger-vdj*, b) when there is a clear dominance
1485 (assessed by difference in UMI count) by a particular contig, and c) if and when there is presence
1486 of one IgM and one IgD contig assigned to a single cell barcode. In the first two cases, the contig
1487 with the highest UMI count is retained; iii) cell barcodes with multiple light chain contigs were
1488 flagged for filtering; iv) in situations where cell barcodes are matched with only light chain contigs,
1489 the contigs would be dropped from the V(D)J data but transcriptome barcode will be retained.

1490

1491 **B cell clone/clonotype definition**

1492 BCRs were grouped into clones/clonotypes based on the following sequential criterion that applies
1493 to both heavy chain and light chain contigs – i) identical V- and J- gene usage, ii) identical
1494 junctional CDR3 amino acid length, and iii) at least 85% amino acid sequence similarity at the

1495 CDR3 junction (based on hamming distance). Light chain pairing is performed using the same
1496 criterion within each heavy chain clone. Only samples collected at day 0 of the study were analyzed
1497 from this step onwards and clones/clonotypes were called across the entire dataset; the sample
1498 from one of the donors who was subsequently found to have a B cell malignancy was separated
1499 from the analysis and processed independently.

1500

1501 **B cell clone/clonotype network**

1502 Single-cell BCR networks were constructed using adjacency matrices computed from pairwise
1503 Levenshtein distance of the full amino acid sequence alignment for BCR(s) contained in every pair
1504 of cells within each disease severity cohort. Construction of the Levenshtein distance matrices
1505 were performed separately for heavy chain and light chain contigs and the sum of the total edit
1506 distance across all layers/matrices was used as the final adjacency matrix. To construct the BCR
1507 neighborhood graph, a minimum spanning tree was constructed on the adjacency matrix for each
1508 clone/clonotype, creating a simple graph with edges indicating the shortest edit distance between
1509 a B cell and its nearest neighbor. Cells with identical BCRs i.e. cells with a total pairwise edit
1510 distance of zero are then connected to the graph to recover edges trimmed off during the minimum
1511 spanning tree construction step. Fruchterman-reingold graph layout was generated using a
1512 modified method to prevent singletons from flying out to infinity in *networkx* (v2.5). Visualisation
1513 of the resulting single-cell BCR network is achieved via transferring the graph to relevant *anndata*
1514 slots, allowing for access to plotting tools in *scanpy*.

1515

1516 The use of the BCR network properties for computing gini indices was inspired from bulk BCR-
1517 seq network analysis methods where distribution of clone sizes and vertex sizes (sum of identical
1518 BCR reads) in BCR clone networks were used to infer the relationships between BCR clonality,
1519 somatic hypermutation and diversity⁷³. However, there are challenges with native implementation
1520 of this approach for single-cell data. Firstly, to enable calculation of network-based clone/cluster
1521 and vertex/node size distribution, BCR networks needed to be reduced such that nodes/cells with
1522 identical BCRs had to be merged and counted; this required the re-construction of BCR networks
1523 per sample and discarding single-cell level information. Furthermore, the process of node
1524 contraction and counting of merging events requires significant computation time and resource.
1525 Secondly, this approach is dependent on sufficient coverage of the BCR repertoire, as the BCRs

1526 from the number of cells sampled (post-QC) may not necessarily recapitulate the entire repertoire,
1527 which may under- or over-represent merged counts for gini index calculation. We propose the use
1528 of node closeness centrality computed on each expanded clone (clone size > 1) as an alternative
1529 metric to emulate the statistics to adapt to the single-cell nature of the data; closeness centrality
1530 defines how close and central each node is with respect to other nodes in the graph and therefore
1531 cells with identical BCRs will have high closeness centrality scores, due to the way the BCR
1532 network is constructed in *dandelion*. Thus, we can quickly calculate if cells across clones, and/or
1533 samples overall, in the entire graph display proportionately/disproportionately high or low
1534 closeness centrality scores. One caveat to the current implementation is that it is only meaningful
1535 if there are clonotypes with at least two cells as scores will only be computed for non-singleton
1536 components of the graph. Gini indices are computed using *skbio.diversity.alpha.gini_index* (*scikit-*
1537 *bio* v0.5.6) with the *trapezoids* method after clone definition and network generation. Summary
1538 visualisation was performed using plotting tools in *seaborn* (v0.11.0).

1539

1540 **Definition of BCR convergence across patients**

1541 BCR overlap was determined by collapsing sharing incidence of V- and J- gene usage and CDR3
1542 amino acid sequences, in both heavy and light chains, between individuals into a binarized format
1543 (1 or 0). The information is turned into an adjacency matrix where an edge is created between two
1544 individuals if there is at least one clonotype (at least 1 cell from each individual displays an
1545 identical combination of heavy and light chain V- and J- gene usage with allowance for somatic
1546 hypermutation at the CDR3 junctional region) that is similar between the two individuals.
1547 Visualisation is achieved using the *CircosPlot* function from *nxviz* package (v0.6.2).

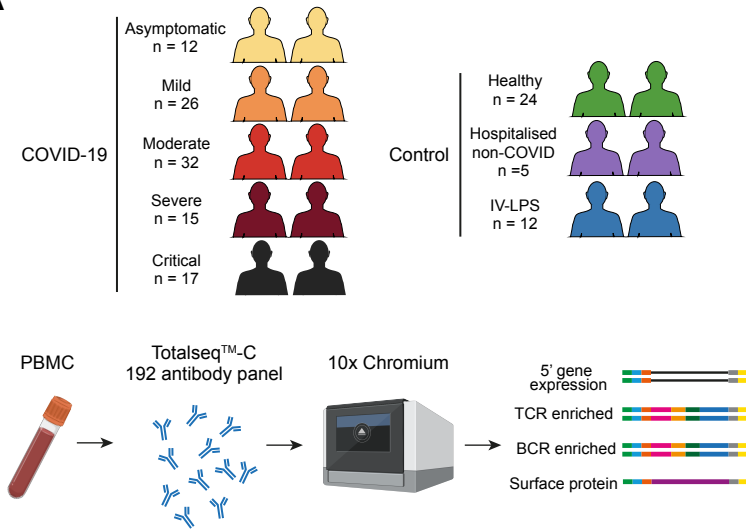
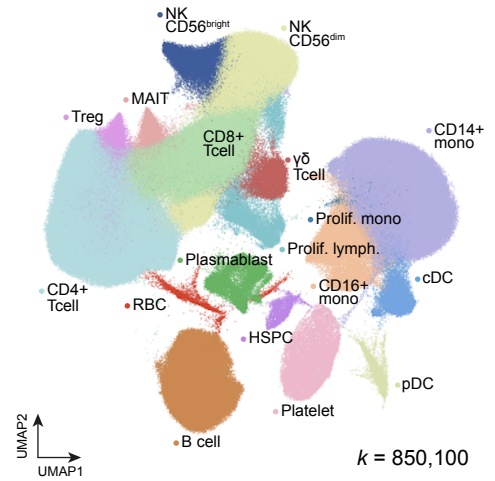
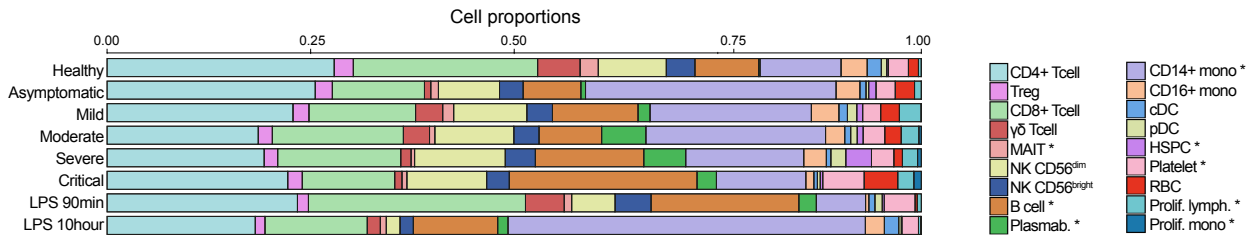
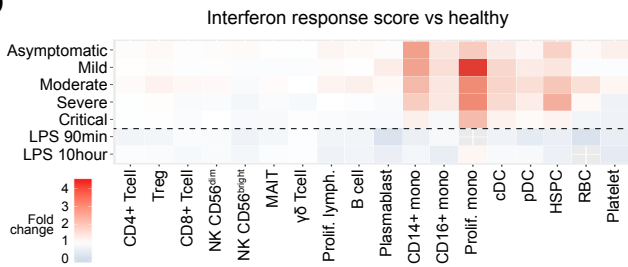
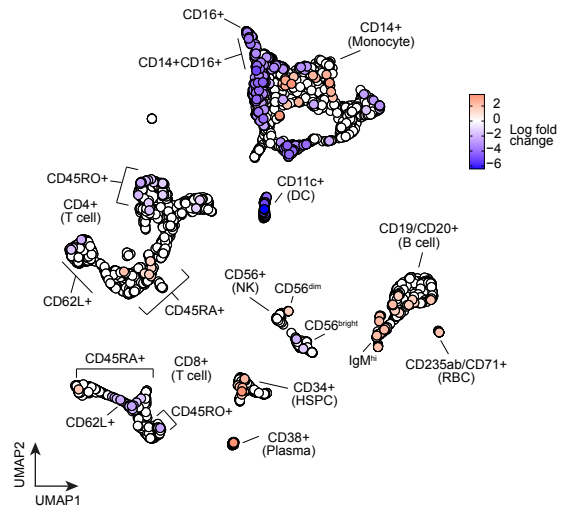
Figure 1**A****B****C****D****E**

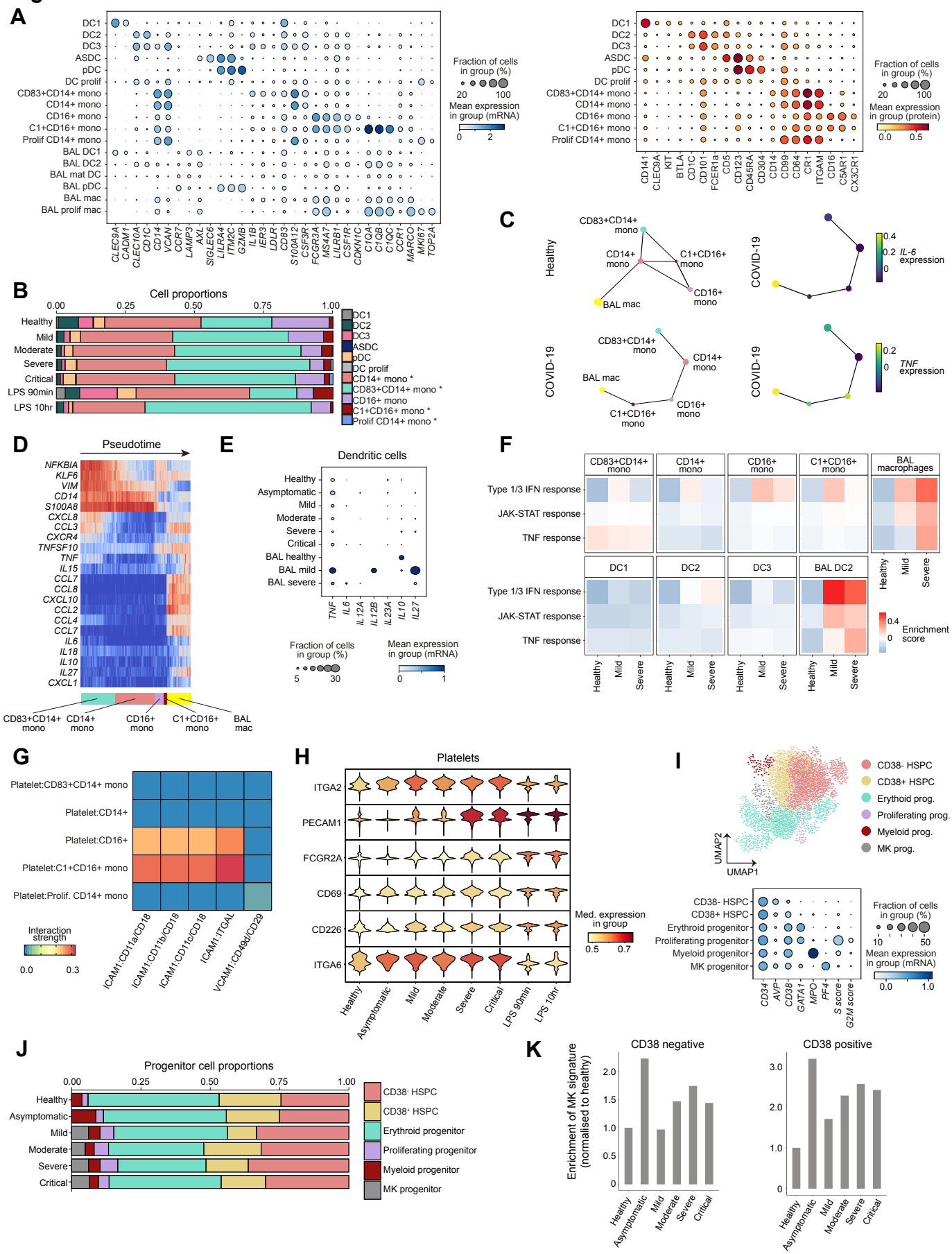
Figure 2

Figure 3

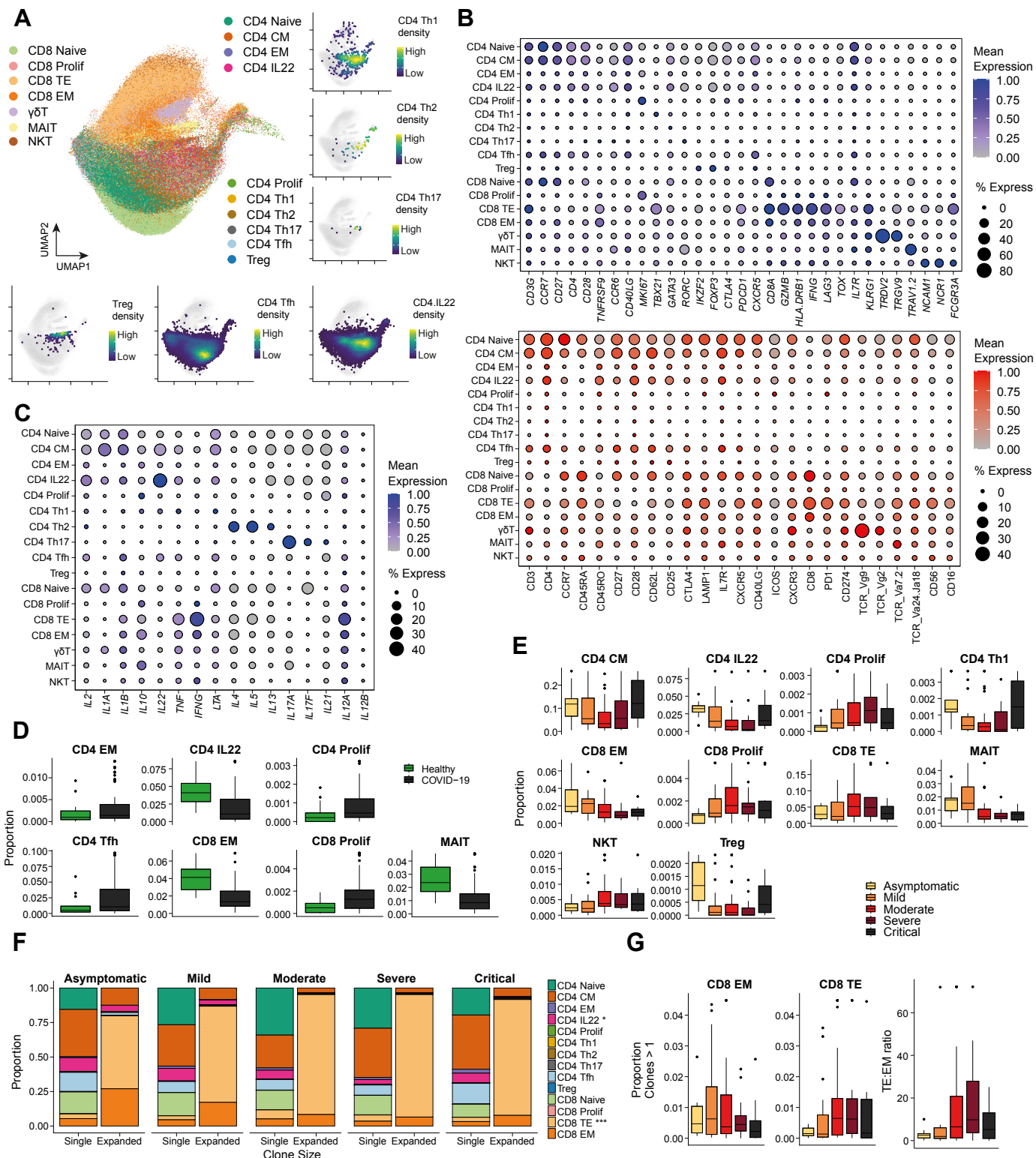


Figure 4

